

Adaptive Integrate-and-Fire Time Encoding Machine with Quantization

Aseel Omar and Alejandro Cohen

Faculty of Electrical and Computer Engineering, Technion—Israel Institute of Technology, Haifa, Israel,
Emails: aseel.omar@campus.technion.ac.il and alecohen@technion.ac.il

Abstract—An integrate-and-fire time-encoding machine (IF-TEM) is a power-effective asynchronous sampler that translates amplitude information into non-uniform time sequences. In this work, we propose a novel Adaptive IF-TEM (AIF-TEM) approach, which dynamically adapts the TEM bias and the induced Nyquist ratio in response to temporal amplitude and frequency variations of the input signal. We provide a comprehensive analysis of AIF-TEM’s oversampling and distortion properties. We also investigate the quantization process for AIF-TEM and analyze the corresponding mean squared error (MSE) bound. Our results show that AIF-TEM achieves significant improvements in rate-distortion performance compared to classical IF-TEM and traditional Nyquist (i.e., periodic) sampling methods for band-limited signals. In particular, AIF-TEM achieves at least a 12 dB reduction in reconstruction MSE under a fixed oversampling rate. When quantization is considered, AIF-TEM provides at least a 14 dB improvement in quantization MSE compared to IF-TEM. Furthermore, AIF-TEM achieves the same reconstruction accuracy using less than 30% of the total bits required by IF-TEM, highlighting the superior efficiency of our adaptive approach. Additionally, we introduce a dynamic quantization technique for AIF-TEM, which further improves performance by at least 10 dB compared to its classical quantization baseline.

Index Terms—asynchronous sampler, integrate-and-fire, time encoding machine, quantization, mean square error.

I. Introduction

CONVENTIONAL analog-to-digital converters (ADCs) transform continuous analog signals into discrete digital values [2]. These ADCs perform two primary operations: periodic sampling and quantization. As depicted in Fig. 1(a), periodic sampling captures the amplitude of the signal at uniform intervals, whereas quantization converts the discrete values of these outcomes into bits [2].

Asynchronous ADCs (AADCs) offer an intriguing alternative due to their energy-efficient operation without the sensitive global clock typically required by traditional ADCs [3]–[5]. In contrast to classic ADCs, AADCs sample signals non-uniformly, only when detecting specific events. In level-crossing asynchronous ADCs (LC-ADCs), sampling occurs when the input signal crosses predefined amplitude thresholds [6]–[8]. While LC-ADCs are widely studied and implemented at the circuit level, particularly for low-power applications, time-encoding approaches differ by triggering sampling when the integral of the input signal reaches a fixed threshold [9]–[12]. Notably,

Parts of this work were presented at the 32nd European Signal Processing Conference, EUSIPCO 2024 [1].

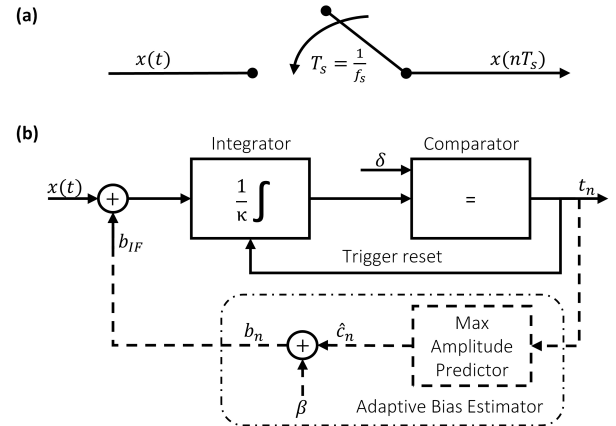


Fig. 1: (a) Periodic Sampler. (b) IF-TEM model (solid lines) and its adaptive design, AIF-TEM (solid with dashed lines).

the density of such time samples is directly related to variations in the signal amplitude [9].

Time encoding offers advantages such as low supply voltage (entirely processed in the time domain), ultra-low power consumption, and a straightforward architecture [12]–[17]. Several implementations of time encoding are available, including the integrate-and-fire time encoding machine (IF-TEM) [17]–[21], and the asynchronous sigma-delta modulator (ASDM) [9], [13], [22], [23]. In practical applications, the output of time encoding machines must be quantized to enable digital processing [9]. However, quantization introduces distortion between the original signal and the signal reconstructed from its quantized samples. Several works have analyzed quantization in time encoding and proposed frameworks to reduce its impact [9], [24]–[26].

In this work, our focus is on the IF-TEM sampler. As depicted in Fig. 1(b) (solid lines), IF-TEM first biases the input analog signal, with a fixed bias, chosen to exceed a constant determined by the signal’s maximal amplitude and frequency. Following this, it integrates and contrasts the result against a threshold and records the instances when this threshold is crossed. However, a primary limitation of the IF-TEM is its fixed bias and resulting constant Nyquist ratio, which do not adapt to variations in signal amplitude and frequency, thereby imposing an oversampling rate [18], [24] that significantly limits its performance. Specifically, its fixed bias is determined by a global amplitude bound, resulting in persistent oversampling when the temporal input signal amplitude is low.

To address this limitation and further optimize time encoding schemes, we introduce a new adaptive design of IF-TEM, termed AIF-TEM, as illustrated in Fig. 1(b). The proposed approach dynamically adjusts its bias in response to variations in the input amplitude and frequency, enabling adaptive adjustments to the actual Nyquist ratio and oversampling rate. The primary objective of this design is to improve efficiency, either by reducing the reconstruction error for a given number of transmitted bits or by reducing the total number of bits required to achieve a target reconstruction quality. The core engineering principle of AIF-TEM is to maintain the adaptive bias close to the temporal maximum amplitude of the signal, while ensuring the reconstruction condition remains satisfied at all times. Our study focuses on analog band-limited (BL) signals to demonstrate the performance benefits of AIF-TEM in both sampling-reconstruction and quantization accuracy.

We thoroughly investigate AIF-TEM's oversampling characteristics and reconstruction distortion from the time-encoded samples, establishing the reconstruction distortion upper bound as a function of the sampling rate in a practical finite regime. This analysis provides deep insights into the effectiveness of our proposed adaptive design.

Additionally, we investigate the AIF-TEM sampler with quantization using a uniform quantizer. We present a tighter upper bound on the quantization MSE for both IF-TEM and its adaptive design. Our results show that adaptive adjustments in AIF-TEM achieve significant performance improvements in a practical finite regime in terms of reconstruction and quantization distortion. We also introduce a dynamic quantization scheme that tracks the step size in a practical finite regime based on the estimated amplitude, thereby reducing the overall distortion of the recovered signals.

Finally, we conducted numerical evaluations using synthetic randomized BL signals and real audio signals to test the sampling process, adopting MSE as our primary evaluation metric. We further evaluated both classic and dynamic quantization schemes. The results demonstrate that AIF-TEM significantly outperforms IF-TEM and periodic sampling methods, both in reconstruction and quantization MSE.

The remainder of this paper is organized as follows: Section II provides essential background information and formulates the problem. In Section III, we detail our proposed AIF-TEM encoding and decoding algorithm and analyze its oversampling characteristics and distortion. We then present numerical simulations testing the sampling and reconstruction process. Section IV analyzes the quantization process, introduces the dynamic quantization strategy, and discusses the distortion of the quantization, followed by numerical simulations comparing the quantization performance of AIF-TEM, IF-TEM, and dynamic quantization for AIF-TEM.

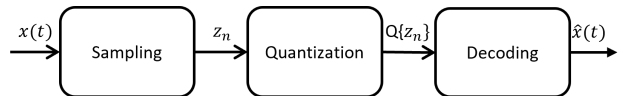


Fig. 2: Generalized signal processing chain comprising time encoding (sampling), quantization, and reconstruction (recovery/decoding).

II. Problem Formulation And Preliminaries

This section introduces the problem formulation and provides background on IF-TEM and periodic samplers.

A. Problem Formulation

We address the problem of sampling an analog signal $x(t)$ and then reconstructing it. We characterize $x(t)$ as follows.

Definition 1. A signal $x(t), t \in \mathbb{R}$ is termed c_{\max} -bounded and 2Ω -BL signal, i.e., band-limited to the frequency support $\mathcal{B} = [-\Omega, \Omega]$, where 2Ω denotes the total bandwidth and Ω is the maximum frequency component, if its amplitude is confined within $|x(t)| \leq c_{\max}$ and its Fourier transform is zero for frequencies outside the closed interval \mathcal{B} .

We assume that $x(t)$ has finite energy E as follows.

Definition 2. A signal $x(t)$ has finite energy $E \in \mathbb{R}$ if

$$E = \int_{-\infty}^{\infty} |x(t)|^2 dt < \infty.$$

Moreover, we consider that for c_{\max} -bounded and 2Ω -BL signal with finite energy E , the amplitude upper bound c_{\max} is related to the bandwidth Ω as derived in [27]

$$c_{\max} = \sqrt{E \frac{\Omega}{\pi}}. \quad (1)$$

Fig. 2 outlines a generalized signal processing chain that encompasses time encoding (sampling), quantization, and reconstruction (recovery/decoding)¹. The input signal $x(t)$ undergoes a sampling process that results in discrete measurements $\{z_n\}_{n \in \mathcal{Z}}$. Sampling may be performed using a conventional sampling method as shown in Fig. 1(a) or through IF-TEM or AIF-TEM methods as shown in Fig. 1(b). After the sampling process, discrete measurements from the sampling stage are quantized to produce bit representations $Q(z_n) = \tilde{z}_n$. The quantized measurements are then decoded to reconstruct the signal $\hat{x}(t)$. In practical scenarios involving finite regimes and quantization, a distortion arises between the original input signal $x(t)$ and the recovered signal $\hat{x}(t)$. This distortion is quanti-

¹We note that in this work, the terms time encoding and sampling are used interchangeably to describe the non-uniform event-based sampling operation of IF-TEM and AIF-TEM. Likewise, the terms reconstruction, recovery, and decoding are used synonymously to denote the inverse operation that reconstructs the input signal from its time-encoded samples.

fied using the Mean Squared Error (MSE), expressed in decibels (dB) as follows

$$\text{MSE} \triangleq 20 \log_{10} \left((1/\sqrt{T}) \|x(t) - \hat{x}(t)\|_{L_2[0,T]} \right) \quad [\text{dB}]. \quad (2)$$

We aim to refine the chain process (see Fig. 2) by reducing the overall reconstruction distortion arising from the entire stages in the chain, for a given number of bits used to quantize the signal, or by reducing the total number of bits required to achieve a target reconstruction distortion.

B. Related Work

Integrate-and-Fire (IF) models are widely used in neuroscience to describe brain activity and neuron spiking behavior [28]. To better mimic neuronal spiking, Leaky IF (LIF) model introduces a leakage term, while the Exponential IF (EIF) model incorporates exponential spike generation [29]. To further capture neural adaptation behavior, the Adaptive Exponential IF (AdEx) model [30] adds an adaptation current that dynamically influences the neuron’s firing rate. In addition, [31] proposed a general adaptation mechanism for LIF neurons. These models primarily aim to prevent excessive neuronal firing. Beyond theoretical neuroscience, several studies [32], [33] have implemented IF models in VLSI circuits, enabling real-time, low-power neuromorphic processing. These hardware-based models emulate biological neurons for neuromorphic computing applications and often include bias currents as part of the neuron dynamics.

While the aforementioned works focus on biological neuron modeling and neuromorphic implementations, where bias terms can be employed (e.g., [34]), their objectives differ from the present work. In neuromorphic systems, the bias typically serves as a neuronal parameter governing firing behavior, whereas in the proposed AIF-TEM (see Section III), it is adaptively controlled to regulate the effective Nyquist ratio and support reconstruction guarantees for bandlimited signals. Unlike AdEx, which adapts spiking dynamics, the proposed method herein derives and adapts the Nyquist condition to ensure perfect signal recovery. It dynamically adjusts event-based sampling to improve the efficiency of analog signal encoding. This is achieved by reducing the overall reconstruction distortion arising from the entire stages in the chain (see Fig. 2), while minimizing bit usage. Our results demonstrate that this adaptive bias enhances signal reconstruction efficiency compared to non-adaptive methods, making it fundamentally distinct from neuroscience-inspired adaptive IF models that focus on capturing neural dynamics, rather than linking their results to the derived adaptive Nyquist requirement suggested herein for BL signals.

Asynchronous Sigma-Delta Modulator (ASDM) was first introduced by [35] as a time encoding scheme based on threshold-triggered integration. Building on earlier integrate-and-fire neuron models (e.g., [36]), Lazar et al. in [18] formalized the Integrate-and-Fire Time Encoding Machine (IF-TEM) framework for bandlimited signal processing and established associated reconstruction

guarantees. Both ASDM and IF-TEM share a common structure, consisting of an adder, an integrator, and a comparator. The key difference between these models lies in that ASDM alternates between positive and negative fixed biases and compares against two thresholds (positive and negative). In contrast, IF-TEM applies only a positive bias and uses a single fixed threshold for comparison. Amplitude Adaptive ASDM (A-ASDM) was introduced in [37] as an extension of ASDM with an adaptive bias mechanism that adjusts based on the time-varying envelope of the signal to reduce power consumption. Later, [38] proposed an A-ASDM design that eliminates explicit envelope encoding while still adapting the bias through a signal-derived function. Further developments in [39] focused on hardware circuit implementations, demonstrating the feasibility of A-ASDM for real-time signal processing.

While A-ASDM primarily focuses on power efficiency and relies on amplitude envelope estimation using the input signal, A-ASDM requires direct access to the analog input waveform. This approach typically involves additional analog circuitry and continuous observation of the signal amplitude. In contrast, the proposed Adaptive IF-TEM detailed in Section III, performs bias adaptation based on amplitude estimates inferred from output event timing without direct access to the input waveform. This enables a fully event-driven architecture that avoids the need for additional analog components. In scenarios where only the event stream is available, such as distributed sensing systems, neuromorphic hardware, or ultra-low-power time-domain implementations, adaptations based on output timings remain applicable and preserve the asynchronous nature of the system. In addition, AIF-TEM introduces a novel adaptive sampling condition based on an analytically derived adaptive Nyquist requirement. The sampling rate is related to the amplitude and frequency variations of the input signal, enabling dynamic control of oversampling while preserving the signal reconstruction guarantees. These contributions result in improved sampling efficiency, reduced quantization error, and a lower number of transmitted bits.

C. IF-TEM vs. Periodic Sampler

Conventional sampling techniques, such as periodic sampling depicted in Fig. 1(a), involve measuring the amplitude of a signal at uniform time intervals. For an input signal $x(t)$, this approach yields discrete samples $x(nT_s)$ with a consistent sampling interval T_s . In contrast, the IF-TEM technique samples $x(t)$ non-uniformly², focusing on capturing time instances rather than amplitude values.

An IF-TEM is characterized by three parameters: a fixed bias b_{IF} , a scaling factor κ , and a threshold δ , as depicted in Fig. 1(b) (solid lines). The input to the IF-TEM, $x(t)$, is a c_{max} -bounded signal. The time-encoding process begins by adding the bias b_{IF} to $x(t)$. This augmented signal, $x(t) + b_{\text{IF}}$, is subsequently scaled by

²Although IF-TEM sampling is inherently non-uniform, some reconstruction approaches map the resulting event times onto a uniform or structured computational grid for recovery; see, e.g., [40].

$1/\kappa$ and integrated. To ensure that the integrator's output continuously rises, it is essential that $b_{\text{IF}} > c_{\text{max}}$. The moments, or firing times, denoted as $\{t_n\}_{n \in \mathcal{Z}}$, are recorded when the integral surpasses the threshold δ . After each recording, the integrator is reset to zero. For $t_n > t_{n-1}$, the integrator's output is given by

$$\frac{1}{\kappa} \int_{t_{n-1}}^{t_n} (x(s) + b_{\text{IF}}) ds = \delta. \quad (3)$$

Thus, the relationship between the input $x(t)$ and its time output $t_n, n \in \mathcal{Z}$ of the IF-TEM is given by

$$P_n \cong \int_{t_{n-1}}^{t_n} x(s) ds = -b_{\text{IF}}(t_n - t_{n-1}) + \kappa\delta. \quad (4)$$

Subsequently, based on [18], the time differences between firing times, denoted as $T_n = t_n - t_{n-1}$, are bounded by

$$\Delta t_{c_{\text{min}}} \triangleq \frac{\kappa\delta}{b_{\text{IF}} + c_{\text{max}}} \leq T_n \leq \frac{\kappa\delta}{b_{\text{IF}} - c_{\text{max}}} \triangleq \Delta t_{c_{\text{max}}}. \quad (5)$$

D. Reconstruction from IF-TEM and Periodic Sampling

For the periodic sampling method, the Shannon-Nyquist theorem dictates that a 2Ω -BL signal, $x(t)$, can be perfectly reconstructed from its discrete samples $x(nT_s)$ when sampled at a rate no less than the Nyquist rate, $\frac{\Omega}{\pi}$ [41].

The recovery of an analog signal from its time-encoded output in IF-TEM has been extensively studied in previous works. Lazar and Tóth [9] proposed an algorithm for the perfect reconstruction of BL and c_{max} -bounded signals from an ASDM sampler. This approach was later extended in [18] to adapt the method for IF-TEM with a refractory period. Subsequently, Lazar et al. in [42], [43] further developed the work in [9] by introducing a real-time recovery algorithm for ASDM output that utilizes a segment-based recovery approach. Moreover, Lazar et al. in [44] proposed a fast recovery algorithm for ASDM.

While these works focused on bandlimited signals, Thao et al. [45] examined various methods for decoding bandlimited signals from leaky IF-TEM output, where the leaky mechanism introduces an additional decay term that affects the timing of threshold crossings. They extended the Projection Onto Convex Sets (POCS) method and compared it to previous decoding approaches. In contrast, Alexandru et al. [46] analyzed the reconstruction of non-bandlimited signals from IF-TEM output, addressing a different class of signals. Recent works such as [47] considered recovery of sparse signals using flexible filter-based time encoding frameworks.

In this work, we adopt the IF-TEM sampling and reconstruction mechanism as outlined in [18] with zero refractory period, which demonstrates that such signals can be perfectly reconstructed using an IF-TEM with parameters $\{b_{\text{IF}}, \kappa, \delta\}$, if $b_{\text{IF}} > c_{\text{max}}$ and the Nyquist ratio, r_c , is given by

$$r_c \triangleq \frac{\kappa\delta}{b_{\text{IF}} - c_{\text{max}}} \frac{\Omega}{\pi} < 1. \quad (6)$$

This constraint stipulates that the interval between two successive trigger times must not exceed the inverse of

the Nyquist rate. We note that the IF-TEM employs a fixed upper-bound bias, setting an average sampling and Nyquist ratio that remains unaffected by variations in the input signal's amplitude and frequency, which significantly limits its performance.

E. Quantization

In classical sampling, each amplitude measurement $z_n = x(nT_s)$ is quantized. Given that these measurements fall within the amplitude range $[-c_{\text{max}}, c_{\text{max}}]$, the quantization step size Δ_{per} for a uniform K -level quantizer is given by

$$\Delta_{\text{per}} = \frac{2c_{\text{max}}}{K}.$$

In contrast, for time encoding machines (TEMs), the sampled output consists of trigger times $z_n = t_n$, which are then quantized. Several works have explored the quantization of time-encoded signals. The authors of [9] studied uniform quantization of time samples from an ASDM and provided a bound on quantization-induced reconstruction distortion. The authors of [26] further investigated ASDM quantization, showing that the sampling density varies with the input signal amplitude, resulting in natural compression or expansion effects. The authors of [25] introduced a model-driven quantization framework for ASDM, proposing the QTEM (Quantized Time Encoding Machine) approach, in which sampling and quantization are combined into a single operation. Their results show that QTEM achieves lower quantization reconstruction distortion compared to conventional uniform quantization.

For IF-TEM, uniform quantization of time samples has been studied in [24], where it is compared against uniform amplitude quantization in classical sampling. The authors derived an upper bound on the quantization mean squared error (MSE) and analyzed how IF-TEM quantization is influenced by signal frequency and amplitude dynamics.

The quantization step size Δ_{IF} for a K -level uniform quantizer is determined based on the dynamic range of the time differences T_n , as follows [24]

$$\Delta_{\text{IF}} = \frac{\kappa\delta}{(b_{\text{IF}} + c_{\text{max}})(b_{\text{IF}} - c_{\text{max}})} \frac{2c_{\text{max}}}{K}. \quad (7)$$

Considering any $\gamma > 1$, let $b_{\text{IF}} = \gamma c_{\text{max}}$, with $b_{\text{IF}} > c_{\text{max}}$. Unlike classical sampling, where increasing the sampling frequency increases the quantization step size, IF-TEM exhibits an inverse relationship between signal frequency and quantization resolution [24]. Specifically, an increase in signal frequency leads to a decrease in the quantization step size Δ_{IF} , since higher frequency signals exhibit larger amplitude variations, affecting inter-event times. The upper bound for the quantization MSE in IF-TEM is given by

$$\mathbb{E}[\mathcal{E}^2]_{\text{IF}} \leq \frac{\Omega(b_{\text{IF}} + c_{\text{max}})}{\pi\kappa\delta} \left(\frac{b_{\text{IF}} + c_{\text{max}}}{1 - r_c} \right)^2 \frac{\Delta_{\text{IF}}^2}{12}. \quad (8)$$

III. AIF-TEM Algorithm

In this section, we introduce the Adaptive Integrate-and-Fire Time Encoding Machine (AIF-TEM), a novel

machine that dynamically adapts its operation to the amplitude and frequency variations of the input. The core idea of AIF-TEM is to adaptively control the sampling rate by modifying the bias b_n based on recent amplitude behavior, allowing better alignment with signal dynamics, unlike classical IF-TEM, which maintains a fixed rate. A key feature of AIF-TEM is the Adaptive Bias Estimator, depicted by dashed lines in Fig. 1(b). This estimator dynamically adjusts the bias b_n to account for variations in signal amplitude. The estimator includes the Max Amplitude Predictor (MAP) block, which estimates amplitude variations and assists in bias adaptation.

Consider a c_{\max} -bounded input signal $x(t)$. For AIF-TEM, the time output is represented as $\{t_n\}, \forall n \in \mathcal{Z}$. In this context, each iteration, represented by n , captures the duration between two successive trigger events, t_{n-1} and t_n . We aim to determine the maximum amplitude value, c_n , within each iteration n . This is achieved by examining a time window that spans from the current trigger time t_n back to the preceding w trigger times. Here, w denotes the number of past trigger intervals in the window. Therefore, the maximum amplitude value c_n within this window is given by

$$c_n \triangleq \max_{t_{n-w} \leq t \leq t_n} (|x(t)|). \quad (9)$$

The MAP block estimates c_n , which is then used to adapt the bias b_n accordingly. To ensure that the integrator output increases consistently, we introduce the following definition.

Definition 3 (Correct MAP Operation). The MAP block operates correctly, ensuring the successful functioning of AIF-TEM, if and only if

$$b_n \geq c_n \quad \forall n \in \mathcal{Z}.$$

Ideally, a desired operational mode ensures that the estimated amplitude \hat{c}_n tracks the temporal maximum amplitude c_n while preserving the adaptive Nyquist condition required for reconstruction (see (13)). This alignment reduces unnecessary oversampling when the signal amplitude is low, while maintaining the sampling density required for accurate recovery when the amplitude increases. Encoding stability is ensured by enforcing $b_n \geq c_n$ (Definition 3), which guarantees monotonic integrator growth. In addition, the bias is constrained within predefined limits, $b_{\min} \leq b_n \leq b_{\max}$, to prevent divergence of the adaptive update and to maintain robustness against estimation errors.

The AIF-TEM algorithm, with a particular emphasis on the bias estimator, supports various operational modes, offering flexibility in how the bias is updated. This adaptability allows AIF-TEM to be optimized for various signal characteristics, opening avenues for further research and improved performance in real-world applications. The subsequent sections detail the encoding process, the implementation of the bias estimator, and alternative operational modes.

A. Encoding Process

The input signal is first biased by b_n , resulting in $x(t) + b_n$. For all $t \in \mathbb{R}$ and $n \in \mathcal{Z}$ with $t \geq t_{n-1}$, the output of the integrator is given by

$$y_n(t) \triangleq \frac{1}{\kappa} \int_{t_{n-1}}^t (x(s) + b_n) ds. \quad (10)$$

Assuming that the MAP block operates correctly as defined in Definition 3, the output $y_n(t)$ will increase monotonically. At time $t = t_n$ (with $t_n > t_{n-1}$), the output $y_n(t)$ reaches the threshold δ , satisfying the relation in (4) with the adaptive bias b_n replacing the fixed bias b_{IF} .

Once t_n is recorded, the integrator resets, and the algorithm uses the time difference $T_n = t_n - t_{n-1}$ to predict the next bias value b_{n+1} .

During the interval $t_{n-1} < t \leq t_n$, the signal's amplitude is constrained by $|x(t)| \leq c_n < b_n$. By leveraging this inequality and substituting it into (4) with the adaptive bias b_n , we determine a bound for the duration between successive trigger times, T_n . This bound is given by

$$\Delta t_{\min}[n] \triangleq \frac{\kappa \delta}{b_n + c_n} \leq T_n \leq \frac{\kappa \delta}{b_n - c_n} \triangleq \Delta t_{\max}[n]. \quad (11)$$

Initially, the bias is set such that $b_{n=1} > c_{\max}$. This configuration ensures that the integrator's output, $y_1(t)$, increases monotonically for all $t \geq t_0$. As a result, $y_1(t)$ surpasses the threshold δ at a time $t_1 > t_0$. Therefore, the equalities in (4) and (11) hold for $n = 1$.

Next, we detail the operation of the Adaptive Bias Estimator, describing our primary mode of operation while briefly outlining alternative approaches.

B. Adaptive Bias Estimator Operation

In this work, we focus on a specific practical and computationally efficient MAP operation mode that demonstrates the effectiveness of the adaptive mechanism in AIF-TEM. In this mode, the bias is updated using the relation $b_n = \hat{c}_n + \beta$, where $\beta > 0$ serves as a safety margin that is chosen to help maintain the condition $b_n \geq c_n$ in Definition 3 in practice, while preserving the Nyquist ratio (discussed in Section III-C).

For amplitude estimation, we adopt an Exponentially Weighted Moving Average (EWMA) filter due to its simplicity, computational efficiency, and ability to track smooth amplitude variations while filtering out noise. These properties make it well-suited for the bandlimited input signals considered in our application. Dividing both sides of (4) by T_n and with the adaptive bias b_n (replacing the fixed bias b_{IF}) yields $\bar{x}_n \triangleq \frac{1}{T_n} \int_{t_{n-1}}^{t_n} x(s) ds = -b_n + \frac{\kappa \delta}{T_n}$, where \bar{x}_n represents the average value of the input signal over the interval (t_{n-1}, t_n) and serves as the amplitude-related quantity used by the MAP block. The estimated amplitude is then computed as

$$\hat{c}_n = \alpha_1 \bar{x}_n + (1 - \alpha_1) \hat{c}_{n-1},$$

where $0 \leq \alpha_1 \leq 1$ is a weighting factor³. To enhance prediction accuracy, we iteratively compute the standard deviation of past estimates, s_n , via Welford's method [48]

$$s_n^2 = \frac{1}{n} \sum_{i=1}^n (\hat{c}_i - \mu_n)^2, \quad \text{where} \quad \mu_n = \frac{1}{n} \sum_{i=1}^n \hat{c}_i.$$

Using this estimate, the next amplitude value is predicted as

$$\hat{c}_{n+1} = \hat{c}_n + \alpha_2 s_n,$$

where α_2 is a weighting factor decided by the user³. Finally, we compute the maximum value among the previous w predicted amplitude values.

The performance of the MAP block in practice is defined as its ability to satisfy the correct MAP operation condition $b_n \geq c_n$ (Definition 3), which guarantees monotonic growth of the integrator and preserves the adaptive Nyquist condition. Since the amplitude estimate \hat{c}_n is obtained herein via causal EWMA filtering and statistical prediction, transient underestimation may occur, potentially yielding $b_n < c_n$. In this case, the integrator may momentarily violate the strict monotonicity condition; however, this event is mitigated in practice by incorporating the design margin parameter β , constraining $b_n \in [b_{\min}, b_{\max}]$, and including the variance-based correction term $\alpha_2 s_n$ in the prediction step. These mechanisms significantly reduce the probability and duration of such events and restore the condition $b_n \geq c_n$ in subsequent iterations. While the considered mode herein may not be optimal in practice, its simplicity enables efficient processing of AIF-TEM, which significantly outperforms existing approaches, as demonstrated in Sections III-E and IV-E. We note that alternative bias estimation approaches exist in the literature, which may offer opportunities for further improvement. Potential alternatives that can meet the requirements in Definition 3 include: 1) Autoregressive with Exogenous Input (ARX) Model – predicts future values based on a linear combination of past values [49]. 2) Kalman Filter – uses a series of time-based measurements to produce optimal estimates of unknown variables [50]. 3) Recursive Least Squares (RLS) – an adaptive filtering algorithm that efficiently updates estimates in real time [51]. We leave the exploration of these methods for future work.

C. Decoding Process

This section outlines the decoding process for a 2Ω BL input signal, $x = x(t), t \in \mathbb{R}$, using the output of AIF-TEM, denoted by $\{t_n\}_{n=0}^N$, with N denotes the total number of samples. The decoding algorithm proposed herein

³The parameters α_1 and α_2 control the adaptation dynamics of the estimator. In the EWMA recursion, values of α_1 close to 1 yield faster tracking with reduced smoothing, whereas smaller values provide stronger smoothing but slower adaptation. The effective memory length of the filter is approximately $1/(1 - \alpha_1)$ samples, which provides a practical guideline for selecting α_1 according to the expected rate of amplitude variation. The parameter α_2 scales the standard-deviation-based correction term and determines the responsiveness of the bias update to amplitude fluctuations.

extends the framework introduced by Lazar [9], [18] and builds upon classical reconstruction techniques employed in non-adaptive TEM schemes [52], [53]. In particular, we adopt a segment-based reconstruction approach, where the decoder dynamically adjusts the bias during reconstruction in accordance with the estimated maximum amplitude observed over the preceding w sampling intervals, as defined in (9). In practical implementation, synchronization between the encoder and decoder is achieved by sharing the adaptive bias update rule and its initialization parameters. In the sampling framework, the adaptive bias sequence b_n is deterministically generated from the time differences T_n via the MAP block described in Section III-B. Since both encoder and decoder implement the same update mechanism with identical initialization, the decoder can regenerate the corresponding bias values.

Thus, the decoding process utilizes \mathcal{S} segments $W_i, i \in [1 : \mathcal{S}]$, each characterized by a continuous interval, $W_i = [t_a, t_b]$. Here, $a = \sum_{k=0}^{i-1} L_k + 1$ and $b = \sum_{k=1}^i L_k$, where L_i denotes the number of discrete sampling times within the i -th segment, starting with $L_0 = 0$. The duration of each window W_i in time is $|W_i| = t_b - t_a$. Let $S_{W_i} = \{a, \dots, b\}$ denote the specific samples within each W_i segment. The total number of samples in the recovery process is given by $N = \sum_i L_i$.

For each i -th segment with $\{b_n\}_{n \in S_{W_i}}$, to decode the signal within each segment W_i from AIF-TEM output, represented by $\{t_n\}_{n \in S_{W_i}}$, we employ the operator \mathcal{A} , defined as

$$\mathcal{A}x = \sum_{n \in S_{W_i}} \int_{t_{n-1}}^{t_n} x(u) du g(t - \theta_n) = \sum_{n \in S_{W_i}} P_n g(t - \theta_n), \quad (12)$$

where $g(t) = \text{sinc}(\Omega t)/\pi t$ is the sinc function, and $\theta_n = (t_{n-1} + t_n)/2$ denotes the midpoints of each pair of consecutive sampling points. This operator distinguishes itself from Lazar's methodology by implementing an adaptive bias. The coefficients $P_n, n \in S_{W_i}$, derived from the sequences $t_n, b_n, n \in S_{W_i}$, as given in (4). The operator \mathcal{A} effectively generates Dirac-delta pulses generated at times θ_n with corresponding weights P_n , and then employs a low-pass filter to smooth these pulses, facilitating the recovery of the bandlimited signal.

Focusing on samples within S_{W_i} for each i -th segment, we define the Nyquist ratio for AIF-TEM as

$$r_{a_n} \triangleq \frac{\kappa \delta}{b_n - c_n} \frac{\Omega}{\pi} < 1, \quad \forall n \in S_{W_i}, \quad (13)$$

and the maximum Nyquist ratio as $r_{w_i} \triangleq \max_{n \in S_{W_i}} \{r_{a_n}\}$.

To recover the signal for $t \in W_i$, we define the sequence $x_l = x_l(t)$ via the recursion $x_{l+1} = x_l + \mathcal{A}(x - x_l)$, starting with $x_0 = \mathcal{A}x$. This recursive approach allows us to refine the signal approximation incrementally. By induction, we deduce that

$$x_l = \sum_{n=0}^l (I - \mathcal{A})^n \mathcal{A}x, \quad (14)$$

where I denotes the identity operator. The recovery process in (14) can be redefined by practical matrices

formulation [18]. In particular, in AIF-TEM, the bias b_n is updated as $b_n = \hat{c}_n + \beta$, where $\beta > 0$ is a safety margin that is chosen to help maintain the condition $b_n \geq c_n$ in Definition 3 in practice. When this condition holds, Lemma 1 implies that the operator $I - \mathcal{A}$ is a contraction on the segment W_i , i.e., $\|(I - \mathcal{A})x\|_{W_i} \leq r_{w_i}\|x\|_{W_i}$ and $r_{w_i} < 1$, which leads to a convergent reconstruction.

D. Analytical Results

This section delves into the performance analysis of the proposed AIF-TEM, focusing first on its oversampling characteristics, followed by an examination of reconstruction distortion as a function of the sampling rate in a practical, finite regime. To maintain clarity in notation, we use the overline symbol \bar{x} to denote the arithmetic mean (average) of a sequence.

Definition 4. [TEM Oversampling] For a 2Ω -BL signal, the average oversampling in TEM is defined as $OS \triangleq f_s \times \frac{\pi}{\Omega}$, where the average sampling frequency, f_s , is given by $f_s \triangleq 1/\overline{T_n}$.

With this definition in place, we now analyze the average oversampling rate of the AIF-TEM and provide a practical upper bound that reflects the influence of its adaptive parameter b_n . The oversampling rate is inversely related to the average time difference between consecutive events, $\overline{T_{n\text{AIF}}}$, which in the AIF-TEM model depends on both the input amplitude c_n and the adaptive bias b_n . Since both b_n and c_n are strictly positive by design, the minimum time difference $\Delta t_{\min}[n]$, defined in Equation (11), is a convex function of these variables.

Applying Jensen's inequality to the convex function $\Delta t_{\min}[n] = \frac{\kappa\delta}{b_n + c_n}$ yields the following lower bound

$$\overline{T_{n\text{AIF}}} \geq \frac{\kappa\delta}{\bar{b}_n + \bar{c}_n} = \frac{\kappa\delta}{\bar{b}_n + \bar{c}_n}. \quad (15)$$

Substituting this result into the oversampling rate expression from Definition 4, we obtain the following upper bound on the average oversampling rate

$$OS_a \leq \frac{\bar{b}_n + \bar{c}_n}{\kappa\delta} \frac{\pi}{\Omega} \leq \frac{\bar{b}_n + c_{\max}}{\kappa\delta} \frac{\pi}{\Omega} \triangleq OSU_a. \quad (16)$$

This bound provides insight into how the adaptive parameter b_n directly impacts the sampling density of the AIF-TEM. As the input amplitude decreases, both b_n and c_n decrease, leading to sparser sampling, which improves efficiency and reduces oversampling.

Reconstruction distortion refers to the discrepancy between the input signal and its reconstructed estimate obtained from the time-encoded samples. Since the time-encoding stage is modeled as ideal in this work [18], [54], [55], the analyzed distortion originates from the reconstruction (decoding) process. This distortion in AIF-TEM is analyzed here as a function of the minimum sampling rate, $f_{s\min} \triangleq \frac{\Omega}{\pi \max_i\{r_{w_i}\}}$. First, we introduce the following two lemmas, which are key steps in upper-bounding this distortion. Before stating the lemmas, we define a tapering function (i.e., a finite-duration window)

used to localize the analysis to a finite segment⁴. For each segment $W_i = [t_s^{(i)}, t_e^{(i)}]$, let $\varphi_i \in C^1(\mathbb{R})$ be a real-valued taper such that $0 \leq \varphi_i(t) \leq 1$, $\varphi_i(t) = 1$ for $t \in W_i$, and $\text{supp}(\varphi_i) \subseteq [t_s^{(i)} - \Delta, t_e^{(i)} + \Delta]$ for some $\Delta > 0$. Hence, the transition region has total width at most 2Δ , and the associated derivative $\varphi_i'(t)$ is supported only near the segment boundaries. The taper function enables a smooth transition between the segment W_i [42], [56], [57]. The leakage term introduced in Lemma 5 depends on these taper properties through both the boundary-transition contribution and the spectral-leakage contribution induced by windowing. These taper-dependent quantities are collected into $\mathcal{J}_{\varphi_i}(x)$ and subsequently propagated into the distortion bound of Theorem 1 via $\mathcal{L}_{\varphi_i}^{\max}(x)$.

Lemma 1. Assume a 2Ω -BL, c_{\max} -bounded signal with finite energy E , sampled using an AIF-TEM. Then, the norm of the discrepancy between x and $\mathcal{A}x$ within W_i is bounded by

$$\|x - \mathcal{A}x\|_{W_i}^2 \leq r_{w_i}^2 \left(\|x\|_{W_i}^2 + \frac{1}{\Omega^2} \mathcal{J}_{\varphi_i}(x) \right).$$

where $\mathcal{J}_{\varphi_i}(u)$ is the leakage term given in Lemma 5 associated with the taper φ_i on W_i .

Lemma 2. Under the same setting as Lemma 1, the difference between x and x_{L_i} for $t \in \mathbb{R}$ is given by $\|x - x_{L_i}\|_{W_i} = \|(I - \mathcal{A})^{L_i+1}x\|_{W_i}$.

Proof: The proofs of Lemmas 1 and 2 are deferred to Appendix D and Appendix E, respectively.

Using Lemmas 1 and 2, the following Theorem provides an upper bound for the reconstruction distortion in the proposed AIF-TEM as a function of the minimum sampling rate. To obtain this bound, we first define the residual sequence $z_k \triangleq (I - \mathcal{A})^k x$ and $\mathcal{J}_i^{\max}(x) \triangleq \max_{0 \leq k \leq L_i} \mathcal{J}_{\varphi_i}(z_k)$ for $k \geq 0$.

Theorem 1. Consider a 2Ω -BL, c_{\max} -bounded signal with finite energy E , sampled using an AIF-TEM. Then the reconstruction distortion as a function of the minimum sampling rate $f_{s\min}$, for maximum Nyquist ratio $r_{w_i} < 1$ in each segment W_i , is upper bounded by

$$\begin{aligned} D_R(f_{s\min}) &\leq \frac{1}{\mathcal{S}} \sum_{i=1}^{\mathcal{S}} \left(r_{w_i}^{2(L_i+1)} \|x\|_{W_i}^2 + \mathcal{L}_{\varphi_i}^{\max}(x) \right) \\ &\leq \frac{1}{\mathcal{S}} \sum_{i=1}^{\mathcal{S}} \left(\left(\frac{\Omega}{\pi f_{s\min}} \right)^{2(L_i+1)} \|x\|_{W_i}^2 + \mathcal{L}_{\varphi_i}^{\max}(x) \right). \end{aligned} \quad (17)$$

where \mathcal{S} is the number of segments, L_i is the number of samples in the i -th segment, and the leakage term defined as

$$\mathcal{L}_{\varphi_i}^{\max}(x) \triangleq \frac{r_{w_i}^2 (1 - r_{w_i}^{2(L_i+1)})}{\Omega^2 (1 - r_{w_i}^2)} \mathcal{J}_i^{\max}(x).$$

⁴In the supplementary material of this work, a discussion is provided on tapering functions in the finite regime in signal processing literature.

Proof of Theorem 1. By Lemma 2,

$$\mathcal{E}_{s_i}^2 \triangleq \|x - x_{L_i}\|_{W_i}^2 = \|(I - \mathcal{A})^{L_i+1}x\|_{W_i}^2 = \|z_{L_i+1}\|_{W_i}^2.$$

Applying Lemma 1 to $z_k = (I - \mathcal{A})^k x$ yields

$$\|z_{k+1}\|_{W_i}^2 = \|z_k - \mathcal{A}z_k\|_{W_i}^2 \leq r_{w_i}^2 \left(\|z_k\|_{W_i}^2 + \frac{1}{\Omega^2} \mathcal{J}_{\varphi_i}(z_k) \right). \quad (18)$$

Using (18) recursively, we obtain

$$\|z_k\|_{W_i}^2 \leq r_{w_i}^{2k} \|x\|_{W_i}^2 + \frac{r_{w_i}^2}{\Omega^2} \sum_{m=0}^{k-1} r_{w_i}^{2m} \mathcal{J}_i^{\max}(x).$$

Now, setting $k = L_i + 1$, we have

$$\|z_{L_i+1}\|_{W_i}^2 \leq r_{w_i}^{2(L_i+1)} \|x\|_{W_i}^2 + \frac{r_{w_i}^2}{\Omega^2} \sum_{m=0}^{L_i} r_{w_i}^{2m} \mathcal{J}_i^{\max}(x),$$

and evaluating the geometric sum yields

$$\|z_{L_i+1}\|_{W_i}^2 \leq r_{w_i}^{2(L_i+1)} \|x\|_{W_i}^2 + \frac{r_{w_i}^2 (1 - r_{w_i}^{2(L_i+1)})}{\Omega^2 (1 - r_{w_i}^2)} \mathcal{J}_i^{\max}(x).$$

Finally, averaging over all segments establishes the first bound in (17). The second bound follows directly since $r_{w_i} \leq \max_j r_{w_j} = \Omega / (\pi f_{s_{\min}})$. \square

As detailed in Lemma 5 and discussed in the supplementary materials of this work, the leakage term $\mathcal{L}_{\varphi_i}^{\max}(x)$ in Theorem 1 arises from the finite windowing operation and consists of two main components. The first component is directly related to the boundary transitions of the taper function $\varphi_i(t)$ and depends on the region where $\varphi_i'(t) \neq 0$. The second component captures spectral leakage introduced by tapering. In the special case where $\varphi_i(t) \equiv 1$ on \mathbb{R} (i.e., $\Delta = 0$), we have $\varphi_i'(t) = 0$ and the transition region is empty. Consequently, all time-domain leakage terms vanish. In particular, leakage becomes small when the plateau region of the window is large relative to the transition width Δ and when the taper varies smoothly. In this regime, the boundary region occupies only a small fraction of the segment, and the inequality in (33) approaches the classical Bernstein bound [42], [56], [57]. In particular, the dependence on the taper regularity, transition width Δ , and boundary behavior is fully absorbed into $\mathcal{J}_{\varphi_i}(x)$ and therefore into $\mathcal{L}_{\varphi_i}^{\max}(x)$ in Theorem 1.

In the corollary below, we express the distortion as a function of the maximum Nyquist ratio r_{w_i} by deriving a bound on L_i based on the average time interval \bar{T}_{W_i} . Formally, we have

$$L_i = \frac{|W_i|}{\bar{T}_{W_i}} \geq \frac{|W_i|}{\max_{n \in S_{W_i}}(T_n)} = \frac{|W_i|}{r_{w_i} \frac{\pi}{\Omega}}. \quad (19)$$

Corollary 1. Assume the setting in Theorem 1. Then, the reconstruction distortion as a function of the maximum Nyquist ratio r_{w_i} in AIF-TEM is upper bounded by

$$D_R(r_{w_i}) \leq \frac{1}{S} \sum_{i=1}^S \left(r_{w_i}^{2 \left(\frac{|W_i|}{r_{w_i}} \frac{\Omega}{\pi} + 1 \right)} \|x\|_{W_i}^2 + \mathcal{L}_{\varphi_i}^{\max}(x) \right).$$

Proof: This corollary follows by substituting the bound on L_i from Equation (19) into the distortion formula in

Equation (17).

Corollary 2. Assume the setting of Corollary 1 and that $r_{w_i} < 1$ for all $i \in [1 : S]$. If the leakage term $\mathcal{L}_{\varphi_i}^{\max}(x) = 0$ for all $i \in [1 : S]$, the reconstruction distortion of AIF-TEM approaches zero as $L_i \rightarrow \infty$, i.e., $D_R \rightarrow 0$, with convergence rate $\mathcal{O}(r_{\max}^{2L_{\min}})$ for $r_{\max} \triangleq \max_{1 \leq i \leq S} r_{w_i} < 1$ and $L_{\min} \triangleq \min_{1 \leq i \leq S} L_i$.

Corollary 2 characterizes the ideal no-leakage case, which is attained, for example, when $\varphi_i(t) \equiv 1$. In finite-window settings with tapering, the leakage term $\mathcal{L}_{\varphi_i}^{\max}(x)$ is generally not exactly zero. Nevertheless, if $\mathcal{L}_{\varphi_i}^{\max}(x) \rightarrow 0$ as $L_i \rightarrow \infty$, then Theorem 1 still implies $D_R \rightarrow 0$. In this more general case, however, the exponential rate $\mathcal{O}(r_{\max}^{2L_{\min}})$ is not guaranteed unless the leakage term decays at least at the same order.

Proof. Under the stated condition $\mathcal{L}_{\varphi_i}^{\max}(x) = 0$, the bound in (17) reduces to

$$D_R \leq \frac{1}{S} \sum_{i=1}^S r_{w_i}^{2(L_i+1)} \|x\|_{W_i}^2.$$

Let $r_{\max} \triangleq \max_{1 \leq i \leq S} r_{w_i} < 1$. Then, for all i , $r_{w_i}^{2(L_i+1)} \leq r_{\max}^{2(L_i+1)}$. Hence, we obtain

$$D_R \leq \frac{1}{S} \sum_{i=1}^S r_{\max}^{2(L_i+1)} \|x\|_{W_i}^2 \leq r_{\max}^{2(L_{\min}+1)} \cdot \frac{1}{S} \sum_{i=1}^S \|x\|_{W_i}^2.$$

Since x has finite energy and the segments $\{W_i\}_{i=1}^S$ are disjoint, we have $\frac{1}{S} \sum_{i=1}^S \|x\|_{W_i}^2 \leq \|x\|^2 < \infty$. Then, because $r_{\max} < 1$, we have $r_{\max}^{2(L_{\min}+1)} \rightarrow 0$ as $L_{\min} \rightarrow \infty$, which implies $D_R \rightarrow 0$. Moreover, the above inequality yields the exponential convergence rate $D_R = \mathcal{O}(r_{\max}^{2L_{\min}})$. \square

The corollary is stated in terms of L_i , the number of samples within segment W_i . Based on (19), we have $L_i = |W_i| / \bar{T}_{W_i}$, where \bar{T}_{W_i} denotes the average time interval within the segment. Applying Definition 4, this can be expressed as $L_i = f_{s,i} |W_i|$, where $f_{s,i}$ denotes the average sampling rate in segment i . Therefore, achieving a target L_i requires selecting the segment duration $|W_i|$ sufficiently large for the expected sampling rate $f_{s,i}$. Furthermore, since the distortion decays exponentially as $\mathcal{O}(r_{w_i}^{2L_i})$, a target distortion level ε can be achieved by enforcing $r_{w_i}^{2L_i} \leq \varepsilon$, which yields the condition $L_i \geq \log(1/\varepsilon) / (2|\log r_{w_i}|)$. Thus, the required number of samples per segment grows only logarithmically with respect to the desired reconstruction accuracy.

E. Evaluation Results for sampling process

This section provides a numerical evaluation of the proposed AIF-TEM, classical IF-TEM, and periodic sampling. The evaluation is conducted using both synthetic signals generated in MATLAB and a real audio signal. For amplitude value estimation, the MAP block model is employed as proposed in Section III-B. The weighting factors are configured as $\alpha_1 = 0.98$ and $\alpha_2 = 0.17$. We

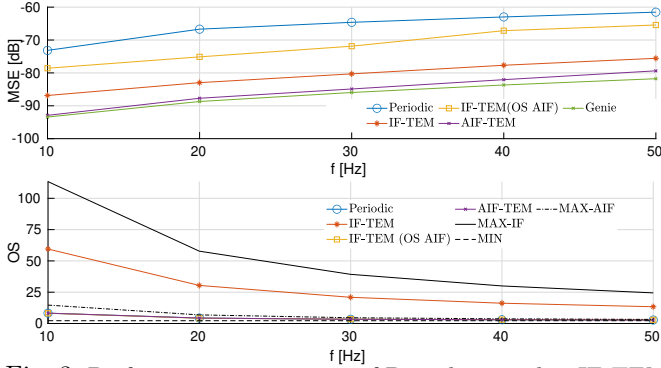


Fig. 3: Performance comparison of Periodic sampler, IF-TEM, AIF-TEM, and 'Genie' sampler in terms of (a) MSE and (b) Oversampling factor (OS).

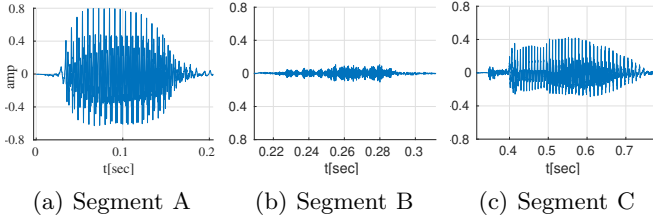


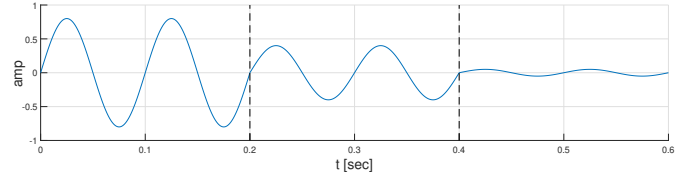
Fig. 4: Comparative performance with audio signal. Each subfigure presents a segment of an audio signal, where under the subfigures, the table represents the MSE in dB of reconstruction for each sampler and the average oversampling factor (OS).

begin by highlighting the advantages of the proposed AIF-TEM using a 2Ω -BL, c_{\max} -bounded signal with finite energy E . Here, $c_{\max} = \sqrt{(E\Omega)/\pi}$ [27], and Ω varies between $2\pi \cdot (10-50)$ Hz. The input signal is defined as

$$x(t) = \sum_{n=-M}^M a[n] \frac{\sin(\Omega(t - n\frac{\pi}{\Omega}))}{\Omega(t - n\frac{\pi}{\Omega})}, \quad (20)$$

where $M = 2$, $t \in \mathbb{R}$, and coefficients $a[n]$ are randomly selected 100 times from $[-1,1]$. The signal energy E is varied within the range $[0.25,2.5]$. For the classical IF-TEM, the bias b_{IF} is set to achieve a Nyquist ratio of $r_c = 0.45$. In the case of AIF-TEM, the safety margin parameter β is chosen such that $r_{a_n} \leq 0.45$ for all n , with a window size $w = 1$.

Fig. 3(a) presents the MSE results as defined in (2). The performance of AIF-TEM is indicated by the purple line, the red line denotes IF-TEM, both are configured with parameters $\kappa = 0.5$ and $\delta = 0.02$. The blue line demonstrates the MSE for periodic sampling, matched to the average sampling frequency of AIF-TEM. The yellow line represents IF-TEM operating with a larger δ , resulting in an average oversampling rate similar to AIF-TEM, which violates the perfect reconstruction condition in (6). The green line demonstrates the MSE for a hypothetical scenario with a "Genie" that informs us of



(a) Segment A (b) Segment B (c) Segment C

	Segment A		Segment B		Segment C	
Sampler	MSE	OS	MSE	OS	MSE	OS
IF-TEM	-86	9	-84	9.2	-91	9.5
AIF-TEM	-106	13	-110	9.2	-102	5.5

Fig. 5: Comparative performance with a bandlimited signal. The table reports the MSE in dB of recovery for each sampler and the average oversampling factor (OS) for each segment.

the temporal amplitude, thereby determining the accurate temporal bias. In Fig. 3(b), the average oversampling for the compared samplers is shown. The black dash-dotted line shows the AIF-TEM maximum oversampling bound from (16). The dark line shows the IF-TEM maximum oversampling, computed by $\frac{\pi/\Omega}{\Delta t_{c_{\min}}}$. In contrast, the dashed line points to the minimum oversampling, based on $1/r_c = 2.22$. Importantly, with similar oversampling, AIF-TEM achieves an MSE reduction of at least 12 dB compared to both IF-TEM and the periodic sampler. Moreover, with the Genie sampler, we observe nearly comparable oversampling and MSE results to those obtained using the estimation block.

Fig. 4 contrasts the performances of the periodic, IF-TEM, and AIF-TEM samplers on a BL audio signal. It's evident that IF-TEM consistently displays a higher oversampling factor, but its MSE performance lags behind AIF-TEM. Notably, AIF-TEM dynamically modulates its oversampling in response to the signal amplitude, resulting in increased oversampling for larger amplitudes. In contrast, the oversampling in IF-TEM remains relatively fixed. When the periodic sampler's rate is aligned with AIF-TEM's oversampling rate, it yields a higher MSE. For IF-TEM2, adjustments to δ ensure that the average oversampling in IF-TEM corresponds to that of AIF-TEM.

Fig. 5 contrasts the performances of IF-TEM and AIF-TEM on a 2Ω -BL signal, $x(t)$ (with $\Omega = 2\pi 10$) that is divided into 3 segments, each with distinct maximum amplitude, $x(t) = a \sin(\Omega t)$, where $a = [0.8, 0.4, 0.05]$ for each segment. The table presents the MSE and the oversampling for each segment.

Figs. 6 and 7 contrast the performances of the IF-TEM and AIF-TEM samplers over time. The input signals are defined by equation (20), characterized by $M = 5$, $\Omega = 2\pi 20$ Hz, and coefficients $a[n]$ randomly selected from $[-1,1]$. Given the signal's maximum energy $E = 0.0869$, we calculate the maximum amplitude as $c_{\max} = \sqrt{(E\Omega)/\pi} = 3.16$. For the AIF-TEM configuration, the parameters are set to $\Delta = 0.01, \kappa = 0.24, \beta = 0.1$ and the MAP block utilizes $w = 5$. For the IF-TEM, the setup involves $\kappa = 0.24$ with a fixed bias $b_{\text{IF}} = c_{\max} + \beta$. To ensure a comparable average oversampling rate to that of AIF-TEM, the threshold δ_c for IF-TEM is adjusted to 0.0433 for the signal presented in Fig. 6(a) and to 0.0262 for the

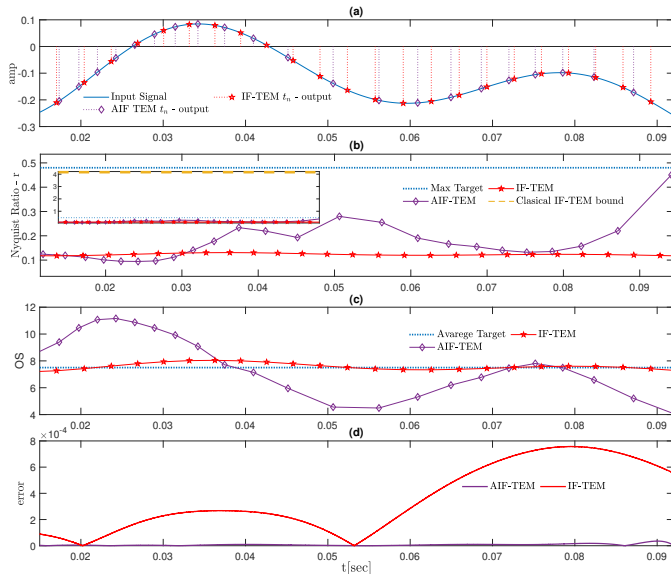


Fig. 6: Time-domain comparison of sampling density and event distribution for AIF-TEM and IF-TEM under varying signal conditions for signal realization 1.

signal presented in Fig. 7(a).

Sub-figures (a) shows the input signals with blue lines, alongside the output times, t_n , of IF-TEM and AIF-TEM, illustrated by Dirac pulses with the same amplitude as the sampled input signal, in red and purple lines, respectively. Sub-figures (b) illustrates the Nyquist ratio, r , with the purple line indicating the ratio for AIF-TEM as per (13) and the red line showing the actual ratio for each time sample of IF-TEM with the fixed bias, i.e., for $b_n = b_{IF}$ (as obtained in practice by the classical scheme in Section II-C). For the ideal case with a genie (such that $b_n = \beta + c_n$), the target Nyquist ratio $r_a = \kappa\delta/\beta$, is depicted by a blue dotted line. The yellow line represents the Nyquist ratio bound, r_c , for IF-TEM as given in (6). Sub-figures (c) compares the oversampling factor of IF-TEM and AIF-TEM, represented by red and purple lines, respectively. These factors are given by $OS_n \triangleq \frac{1}{T_n} \times \frac{\pi}{\Omega}$, where the blue dotted line indicates the mean oversampling as in Definition 4. The oversampling results, presented for both samplers, are for $T_n = t_{n+1} - t_n$, using the output times illustrated in Sub-figures (a). Sub-figures (d) presents the reconstruction error between the input signals and recovered signals from IF-TEM and AIF-TEM outputs, showcased by red and purple lines, respectively. The error metric shown is $|x(t) - \hat{x}(t)|$, where $\hat{x}(t)$ denotes the recovered signal. In the scenario presented in Fig. 6, the MSE values in dB are -103.78 for AIF-TEM and -70.4 for IF-TEM. Additionally, for sampling using a periodic sampler, with a sampling frequency and oversampling rate equivalent to the average determined by AIF-TEM, the MSE value in dB is -48.27 . Similarly, for Fig. 7, the MSE values are -109.14 for AIF-TEM, -79.78 for IF-TEM, and -69.75 for periodic sampler.

We do note, that sub-figures (b) reveals that the Nyquist ratio for IF-TEM at each time sample significantly deviates from the classical IF-TEM bound (given in (6)). This

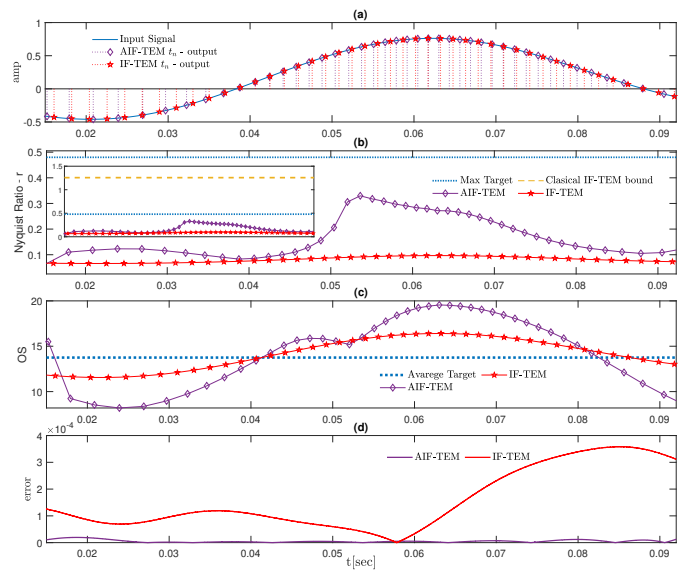


Fig. 7: Time-domain comparison of sampling density and event distribution for AIF-TEM and IF-TEM under varying signal conditions for signal realization 2.

deviation is attributed to the fixed bias, which exceeds the maximum amplitude value and lacks adaptation to temporal amplitude variations. Conversely, AIF-TEM dynamically adjusts its bias in response to temporal amplitude values, c_n , and the standard deviation of the preceding values, following the proposed adaptive scheme with the MAP block. This adjustment ensures that the Nyquist ratio is adapted to amplitude changes. Furthermore, Sub-figures (c) demonstrate that AIF-TEM's oversampling, at each time sample, is responsive to amplitude fluctuations compared to IF-TEM. For IF-TEM, the oversampling rates for each time sample remain near to the average oversampling, showing less adaptability.

In summary, it is important to note that the observations from Figs. 6 and 7 illustrate that IF-TEM's sampling behavior does not adapt to variations in the signal amplitude and frequency, resulting in a constant Nyquist ratio and oversampling rate. In contrast, the proposed AIF-TEM's adaptive bias mechanism, by MAP block, allows for adjustments in the Nyquist ratio and oversampling rate in response to signal variations, showcasing its adaptability and results with significantly lower error in the scenarios evaluated. Finally, we extend the evaluation presented in this section to support overlapping between encoded segments, as commonly adopted in real-time applications, by incorporating tapering functions, i.e., finite-duration windows [56], [57] (see Section III-D and the supplementary materials for the analytical justification). In the tests, the signal is divided into segments of length $0.2s$ with overlap width $\Delta = 0.02s$ at each boundary. Specifically, each segment $W_i = [t_s^{(i)}, t_e^{(i)}]$ is multiplied by a cosine taper whose plateau equals one on $[t_s^{(i)} + \Delta, t_e^{(i)} - \Delta]$, with smooth transition regions of total width 2Δ at the segment boundaries. This overlap-add strategy follows the same framework used in [42]. In our simulations, the MSE difference between the non-tapered

reconstruction and the tapered overlap-add reconstruction remained within approximately 3–4 dB across all samplers tested. Importantly, the relative performance gains of AIF-TEM over IF-TEM were preserved under tapering, confirming that the adaptive advantages remain robust in finite-duration, overlap-add implementations.

In the following sections, we delve into the analysis of quantization for AIF-TEM.

IV. Quantization for AIF-TEM

Following the sampling stage using AIF-TEM, we proceed to quantize the time differences, $T_n = t_{n+1} - t_n$. The quantized time differences are denoted by $\tilde{T}_n = \tilde{t}_{n+1} - \tilde{t}_n$. While the biases b_n are utilized in the signal recovery process, they are selected from a predefined discrete set with resolution Δ_b over the range $[b_{\min}, b_{\max}]$ and are not further quantized beyond this resolution. The MAP block updates b_n according to the amplitude estimate c_n , as described in Section III-B. We represent each bias value by its index on the known grid, $k_n \triangleq \frac{b_n - b_{\min}}{\Delta_b} \in \{0, 1, \dots, K_b - 1\}$, for $K_b \triangleq \left\lceil \frac{b_{\max} - b_{\min}}{\Delta_b} \right\rceil$. Accordingly, the bias information can be conveyed to the decoder by transmitting the index sequence $\{k_n\}$ aligned with the event stream, which requires $R_b = \lceil \log_2 K_b \rceil$ bits per bias index. Since b_{\min} , b_{\max} , and Δ_b are shared between encoder and decoder, each received index uniquely determines the corresponding bias value via $b_n = b_{\min} + k_n \Delta_b$, thereby ensuring synchronization during reconstruction.

This section delineates two quantization schemes for AIF-TEM: 1) a dynamic uniform quantizer that adjusts the step size Δ_{W_i} , per segment W_i , and 2) a classic uniform quantizer with a fixed step size Δ . These schemes are detailed in Subsections IV-A and IV-B and illustrated in Fig. 8.

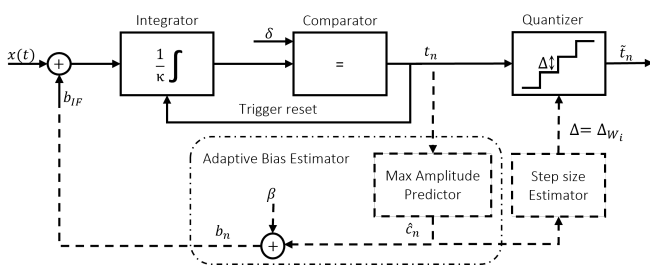


Fig. 8: IF-TEM (solid lines) and its adaptive design, AIF-TEM (solid with dashed lines), with classic and dynamic quantization schemes.

In the following subsection, we elaborate on dynamic quantization.

A. Dynamic Quantization

The dynamic approach uses a K -level uniform quantizer with dynamically adjusted quantization step sizes for each individual segment i . The step size varies for every segment W_i , based on the maximum bias and maximum amplitude, determined as $b_{\max}^{(i)} = \max\{b_n \mid n \in S_{W_i}\}$ and $c_{\max}^{(i)} = \max\{c_n \mid n \in S_{W_i}\}$, respectively. The decoder

identifies the segment boundaries according to the shared deterministic segmentation rule described in Section III-C. Since the quantization step size Δ_{W_i} is computed at the encoder based on segment-specific statistics, its value is signaled once per segment as side information using a fixed predefined representation. This ensures that both encoder and decoder apply identical quantization parameters within each segment. The objective of dynamic quantization for AIF-TEM is to reduce the step size, thereby minimizing the overall distortion in the recovered signal. This approach is particularly beneficial for signals with amplitude and frequency variations. The following lemma introduces the quantization step size for each segment.

Lemma 3. Consider an AIF-TEM with a correctly operating MAP block, followed by a K -level dynamic uniform quantizer. For a c_{\max} -bounded signal, the quantization step size Δ_{W_i} in each segment i is given by

$$\Delta_{W_i} = \kappa \delta \frac{b_{\max}^{(i)} + c_{\max}^{(i)} - \beta}{\beta(b_{\max}^{(i)} + c_{\max}^{(i)})K}. \quad (21)$$

Proof. Using (11), the lower bound for time differences in the i -th segment, $T_n, \forall n \in S_{W_i}$, is given by

$$\Delta t_{\min}[n] = \frac{\kappa \delta}{b_n + c_n} \geq \frac{\kappa \delta}{b_{\max}^{(i)} + c_{\max}^{(i)}} = T_{\min}^{(i)}, \quad (22)$$

when the inequality follows from the definition of $b_{\max}^{(i)}$ and $c_{\max}^{(i)}$. The upper bound for time differences in the i -th segment is given by

$$\begin{aligned} \Delta t_{\max}[n] &= \frac{\kappa \delta}{b_n - c_n} \leq \frac{\kappa \delta}{\min_n \{b_n - c_n\}} \\ &\leq \frac{\kappa \delta}{\beta} = T_{\max}^{(i)}, \end{aligned} \quad (23)$$

where the first inequality holds directly, and the last inequality follows from Definition 3, i.e., $b_n \geq c_n$. Thus, in the segment i , the dynamic range of $T_n, \forall n \in S_{W_i}$ is given by

$$T_{\max}^{(i)} - T_{\min}^{(i)} = \kappa \delta \frac{b_{\max}^{(i)} + c_{\max}^{(i)} - \beta}{\beta(b_{\max}^{(i)} + c_{\max}^{(i)})}, \quad (24)$$

and the quantization step is $\Delta_{W_i} = (T_{\max}^{(i)} - T_{\min}^{(i)})/K$. \square

While the MAP block in practical scenarios may not estimate the amplitude perfectly, in the numerical evaluation we use the estimated maximum amplitude for the i -th segment, $\hat{c}_{\max}^{(i)} = \max\{\hat{c}_n\}, n \in S_{W_i}$.

We note that in the suggested dynamic quantization approach herein, each segment i includes side information containing either the segment's maximum amplitude and bias or the computed step size Δ_{W_i} . This side information informs the decoder how to interpret the quantized levels for that segment. Although Δ_{W_i} varies across segments, the total number of quantization levels K (and thus $\log_2(K)$ bits per sample) can remain the same for all segments. Since Δ_{W_i} depends inversely on $c_{\max}^{(i)}$, as seen in (21), segments with lower amplitudes result in smaller

step sizes, thereby reducing quantization distortion in those regions. As shown in the simulation results in Section IV-E, for three signal segments (and thus four distinct step sizes), the amount of side information is small, yet it yields a significantly smaller reconstruction error. Hardware deployment of this approach would require dedicated protocols to transmit or store side information, which we leave for future work.

B. Classic Quantization

This traditional approach applies a uniform quantizer with a constant step size across all segments. Since $c_{\max}^{(i)} \leq c_{\max}$ for all i , and the MAP block always assigns $b_n \leq b_{\max}$ for all n , it follows that $b_{\max}^{(i)} \leq b_{\max}$ for every segment i . Substituting these inequalities into (22) and noting that $T_{\max}^{(i)}$ is fixed across all segments, we obtain the quantization step size for the classic K -level uniform quantizer as

$$\Delta = \kappa\delta \frac{b_{\max} + c_{\max} - \beta}{\beta(b_{\max} + c_{\max})K}. \quad (25)$$

As an example, if the maximum bias is set to $b_{\max} = \beta + c_{\max}$ with a fixed β , then the quantization step Δ increases with the maximum signal amplitude c_{\max} . In contrast, if the bias is scaled as $b_{\max} = \gamma c_{\max}$ for some $\gamma > 1$, then Δ decreases as c_{\max} increases, thereby improving quantization resolution in high-amplitude regions. This behavior aligns with the result in [24, Theorem 1], where the authors showed that for IF-TEM, increasing the signal's frequency or finite energy—both of which raise c_{\max} —leads to a smaller quantization step size.

C. Upper Bound for Quantization Error

We delve into the analysis of the MSE upper bound between the signal reconstructed from quantized time-encoded samples and the original input signal, $x(t)$. The total reconstruction distortion is decomposed into two components: the reconstruction distortion D_R , corresponding to reconstruction from the non-quantized sampler output, and the quantization distortion D_Q , corresponding to the additional error introduced by quantization of the time intervals.

In the following, we establish an upper bound for the quantization distortion D_Q . This analysis follows methodologies similar to those used in [9] and applies to both dynamic and classic (fixed step size) quantization schemes. We denote the quantization step size as Δ_i for each segment i . In the classical approach, Δ_i remains constant across all segments, i.e., $\Delta_i = \Delta$. In the dynamic approach, the step size Δ_i varies for each segment, i.e., $\Delta_i = \Delta_{W_i}$.

For each segment W_i , we consider the signal

$$x_{d_i}(t) = \sum_{k=0}^{L_i} (I - \tilde{\mathcal{A}})^k \tilde{\mathcal{A}}x, \quad (26)$$

where $\tilde{\mathcal{A}}$ is given by

$$\tilde{\mathcal{A}}x = \sum_{n \in S_{W_i}} \int_{\tilde{t}_{n-1}}^{\tilde{t}_n} x(u) du g(t - \tilde{\theta}_n),$$

and $\tilde{\theta}_n = (\tilde{t}_{n-1} + \tilde{t}_n)/2$. The reconstructed signal from the quantizer output is given by

$$x_{q_i}(t) = \sum_{k=0}^{L_i} (I - \tilde{\mathcal{A}})^k \sum_{n \in S_{W_i}} (\kappa\delta - b_n \tilde{T}_n) g(t - \tilde{\theta}_n). \quad (27)$$

While the equality described in (4) holds at the sampler output, the quantization process disrupts it. Specifically, $\int_{\tilde{t}_{n-1}}^{\tilde{t}_n} x(u) du \neq \kappa\delta - b_n \tilde{T}_n$, which introduces quantization distortion. We denote the signal reconstructed from the sampler output in segment i as $x_{s_i}(t)$, which corresponds to x_{L_i} as defined in (14), where $l = L_i$, and L_i is the number of samples in the i -th segment.

For a sufficiently large segment W_i , and assuming $\mathcal{S} = 1$, perfect reconstruction is achievable from the non-quantized AIF-TEM output, as suggested by Corollary 2. In particular, when L_i is sufficiently large, the reconstructed signal from the sampler output satisfies $x_{s_i}(t) \rightarrow x(t)$. In this regime, the signal $x_{d_i}(t)$, defined in (26), provides a good approximation of $x_{s_i}(t)$. Consequently, the quantization distortion can be analyzed by studying the difference between the signals $x_{q_i}(t)$ and $x_{d_i}(t)$. However, for finite W_i lengths, the signal reconstructed from the sampler output, $x_{s_i}(t)$, does not exactly match the original input $x(t)$ within the segment, giving rise to reconstruction distortion, which was analyzed in Section III-D. For these cases, we assume $x_{d_i}(t) \approx x_{s_i}(t)$, with the reconstruction distortion relative to the input $x(t)$ elaborated in Theorem 1.

The following lemma provides an upper bound on the quantization MSE for segment i , defined as the MSE between $x_{q_i}(t)$ and $x_{s_i}(t)$. The analysis of the lemma adopts the classical high-resolution quantization model, in which the quantization error is modeled as an i.i.d. uniform sequence independent of the signal. While adjacent time samples generated from bandlimited signals exhibit correlation, this approximation is standard in high-resolution quantization theory and is widely used in time-encoding and sampling analyses (e.g., [9], [24]).

Lemma 4. Assume the quantization error for some $n \in S_{W_i}$ by $d_n = \tilde{T}_n - T_n$ is a sequence of i.i.d. random variables in $[-\Delta_i/2, \Delta_i/2]$. Then, the MSE of the reconstructed signal from the AIF-TEM quantized times output in the i -th segment is bounded by

$$\mathbb{E}[\mathcal{E}_q^2]_i \leq \frac{(1 - r_{w_i}^{L_i+1})^2}{(1 - r_{w_i})^2} \frac{(\Delta_i \kappa \delta)^2}{12} \frac{\Omega}{\pi} \left(\frac{1}{T_n} \right)_i^3. \quad (28)$$

Proof. The MSE for segment i is given by

$$\mathbb{E}[\mathcal{E}_q^2]_i = \frac{1}{|W_i|} \mathbb{E} [\|x_{q_i}(t) - x_{s_i}(t)\|_{W_i}^2].$$

Substituting (26) and (27) leads to

$$\mathbb{E}[\mathcal{E}_q^2]_i = \frac{1}{|W_i|} \mathbb{E} \left[\left\| \sum_{k=0}^{L_i} (I - \tilde{\mathcal{A}})^k \sum_{n \in S_{W_i}} \epsilon_n g(t - \tilde{\theta}_n) \right\|_{W_i}^2 \right],$$

where,

$$\epsilon_n = (\kappa\delta - b_n \tilde{T}_n) - \int_{\tilde{t}_{n-1}}^{\tilde{t}_n} x(u) du.$$

Now, we upper bound the MSE. Using $\|v\|_{W_i} \leq \|v\|_2$, we obtain

$$\begin{aligned} \mathbb{E}[\mathcal{E}_q^2]_i &\leq \frac{1}{|W_i|} \mathbb{E} \left[\left\| \sum_{k=0}^{L_i} (I - \tilde{\mathcal{A}})^k \sum_{n \in S_{W_i}} \epsilon_n g(t - \tilde{\theta}_n) \right\|_2^2 \right] \\ &\stackrel{(a)}{\leq} \left\| \sum_{k=0}^{L_i} (I - \tilde{\mathcal{A}})^k \right\|_2^2 \frac{1}{|W_i|} \mathbb{E} \left[\left\| \sum_{n \in S_{W_i}} \epsilon_n g(t - \tilde{\theta}_n) \right\|_2^2 \right] \\ &\stackrel{(b)}{\leq} \frac{(1 - r_{w_i}^{L_i+1})^2}{(1 - r_{w_i})^2} \frac{1}{|W_i|} \mathbb{E} \left[\left\| \sum_{n \in S_{W_i}} \epsilon_n g(t - \tilde{\theta}_n) \right\|_2^2 \right] \\ &\stackrel{(c)}{=} \frac{(1 - r_{w_i}^{L_i+1})^2}{(1 - r_{w_i})^2} \frac{1}{|W_i|} \int_{-\infty}^{\infty} \sum_{n, m \in S_{W_i}} g(t - \tilde{\theta}_n) g(t - \tilde{\theta}_m) \mathbb{E}[\epsilon_n \epsilon_m] dt \\ &\stackrel{(d)}{=} \frac{(1 - r_{w_i}^{L_i+1})^2}{(1 - r_{w_i})^2} \frac{1}{|W_i|} \sum_{n \in S_{W_i}} \left(\frac{\kappa\delta}{\tilde{T}_n} \right)^2 \frac{\Delta_i^2}{12} \int_{-\infty}^{\infty} g^2(t - \tilde{\theta}_n) dt \\ &\stackrel{(e)}{\leq} \frac{(1 - r_{w_i}^{L_i+1})^2}{(1 - r_{w_i})^2} \frac{\Omega(\Delta_i \kappa \delta)^2}{12\pi} \frac{1}{L_i \tilde{T}_n} \sum_{n \in S_{W_i}} \left(\frac{1}{\tilde{T}_n} \right)^2 \\ &\stackrel{(f)}{\leq} \frac{(1 - r_{w_i}^{L_i+1})^2}{(1 - r_{w_i})^2} \frac{\Omega(\Delta_i \kappa \delta)^2}{12\pi} \overline{\left(\frac{1}{\tilde{T}_n} \right)_i^3}, \end{aligned}$$

where (a) follows from the norm properties, i.e., $\|Tv\|_2 \leq \|T\|_2 \|v\|_2$. (b) follows from Lemma 7 applied in $L^2(\mathbb{R})$, which yields $\|(I - \tilde{\mathcal{A}})v\|_2 \leq r_{w_i} \|v\|_2$ for signals generated from the sample set S_{W_i} . Therefore, $\|(I - \tilde{\mathcal{A}})^k\|_2 \leq r_{w_i}^k$, and the operator-sum norm is bounded by the geometric series $\sum_{k=0}^{L_i} r_{w_i}^k = \frac{1 - r_{w_i}^{L_i+1}}{1 - r_{w_i}}$. (c) follows directly by applying the norm. (d) follows since $\mathbb{E}[\epsilon_n \epsilon_m] = \left(\frac{\kappa\delta}{\tilde{T}_n} \right)^2 \frac{\Delta_i^2}{12} \delta_{n,m}$ (the proof is given in Appendix F1), and by interchanging the sum and the integral. (e) follows from Parseval's theorem and the bandlimited spectrum of $g(t)$, $\int_{-\infty}^{\infty} g^2(t - \eta) dt = \frac{1}{2\pi} \int_{-\infty}^{\infty} 1_{[-\Omega, \Omega]} dw = \frac{\Omega}{\pi}$, and substituting $|W_i| = L_i \tilde{T}_n$ for $n \in S_{W_i}$. (f) By the inequality

$$\left(\frac{1}{\tilde{T}_n} \right) \overline{\left(\frac{1}{\tilde{T}_n} \right)^2} \leq \overline{\left(\frac{1}{\tilde{T}_n} \right)^3} \quad (\text{Proof in Appendix F2}),$$

we immediately obtain the desired bound. \square

Next, we establish an upper bound for the quantization MSE by utilizing the temporal biases b_n and the temporal amplitudes c_n .

Corollary 3. Assume the setting in Theorem 4. Then the MSE of the reconstructed signal from AIF-TEM quantized times output in the i -th segment is bounded by

$$\mathbb{E}[\mathcal{E}_q^2]_i \leq \frac{(1 - r_{w_i}^{L_i+1})^2}{(1 - r_{w_i})^2} \frac{\Delta_i^2}{12} \frac{\Omega}{\pi} \frac{(\overline{b_n + c_n})_i^3}{\kappa\delta}. \quad (29)$$

Proof. By substituting the lower bound of (15) with \overline{T}_n

for $n \in S_{W_i}$ into equation (28), we obtain the desired result. \square

The total quantization distortion, D_Q , for segments with maximum Nyquist ratio $r_{w_i} < 1$, is upper bounded by the average of the segment-wise quantization MSE values

$$D_Q \leq \frac{1}{S} \sum_{i=1}^S \mathbb{E}[\mathcal{E}_q^2]_i. \quad (30)$$

In summary, the total distortion, D_T , is upper bounded by the sum of the average reconstruction distortion across all segments (see Subsection III-D) and the additional distortion introduced by quantization. That is,

$$D_T \leq D_R + D_Q,$$

where D_R is given in (17).

Remark 1. The analytical results of this section also apply to IF-TEM with fixed parameters instead of the adaptive parameters for the AIF-TEM.

Remark 2. For a sufficiently large segment, applying the fixed parameters for IF-TEM ($b_n = b_{\text{IF}}$, $r_{w_i} = r_c$, $c_n = c_{\text{max}}$) to the bound in (29), we obtain the bound provided in (8), as presented by [24].

D. Comparison to IF-TEM

This section compares the oversampling of AIF-TEM and IF-TEM, and relates it to the quantization MSE of both samplers. Let OS_c denote the oversampling of IF-TEM and OSU_c denote its upper bound. By applying the fixed bias b_{IF} to (16), we obtain $OS_c \leq \frac{b_{\text{IF}} + c_{\text{max}}}{\kappa\delta} \frac{\pi}{\Omega} \triangleq OSU_c$. Let f_{s_a} and f_{s_c} denote the average sampling frequencies for AIF-TEM and IF-TEM, respectively. From Definition 4 and Eq. (15), we get $f_{s_a} \leq \frac{\tilde{b}_n + \tilde{c}_n}{\kappa\delta}$ and by applying the fixed bias and maximum amplitude b_{IF} and c_{max} , we have $f_{s_c} \leq \frac{b_{\text{IF}} + c_{\text{max}}}{\kappa\delta}$. The following proposition compares the oversampling rates of AIF-TEM and IF-TEM.

Proposition 1. Let $x = x(t)$, $t \in \mathbb{R}$, be a 2Ω -BL signal with $|x(t)| \leq c_{\text{max}} < \infty$. Assume $x(t)$ is sampled using an IF-TEM characterized by parameters $b_{\text{IF}} > c_{\text{max}}$, κ , and δ , and an AIF-TEM with shared parameters κ and δ and a correct operating MAP. For $b_n \leq b_{\text{IF}}, \forall n$, then $f_{s_a} \leq f_{s_c}$ and $OS_a \leq OS_c$.

Proof. Given the successful operation of MAP and $b_n \leq b_{\text{IF}}$, we have, $x(t) + b_n \leq x(t) + b_{\text{IF}}$. With fixed κ and δ , and referencing (10) and (3), the output of the AIF-TEM integrator reaches the threshold δ more slowly than the IF-TEM. This results in larger time intervals, leading to a reduced average sampling frequency and oversampling for AIF-TEM. \square

Remark 3. Under the conditions of Proposition 1, the quantization MSE bound given in (29) for AIF-TEM is smaller than that of IF-TEM. This improvement arises because the adaptive bias b_n in AIF-TEM is typically

smaller than the fixed worst-case bias b_{IF} used in IF-TEM, resulting in a reduced quantization error bound.

Let ν denote the oversampling ratio between IF-TEM and AIF-TEM, defined as $\nu = OS_c/OS_a$, and let ρ be the number of bits used to encode the bias. The following proposition shows that, under certain conditions, AIF-TEM requires fewer total bits to encode the signal than IF-TEM.

Proposition 2. Consider IF-TEM and AIF-TEM configured as in Proposition 1, followed by a K -level dynamic uniform quantizer. The total number of bits used to encode the signal is smaller for AIF-TEM if $\nu - 1 \geq \frac{\rho}{\log_2 K}$. In this case, the ratio of total bits between IF-TEM and AIF-TEM is given by

$$r_{\text{bits}} = \frac{\nu \log_2 K}{\log_2 K + \rho}. \quad (31)$$

Proof. Let L_a denote the number of samples generated by AIF-TEM. Then IF-TEM produces νL_a samples. With a K -level dynamic uniform quantizer, the total number of bits for IF-TEM is $\nu L_a \log_2 K$, where $\nu \geq 1$ as shown in Proposition 1.

For AIF-TEM, the total number of bits is $L_a \log_2 K + \rho L_a$. Hence, the ratio of total bits is

$$r_{\text{bits}} = \frac{\nu L_a \log_2 K}{L_a (\log_2 K + \rho)}.$$

Dividing the numerator and the denominator by L_a yields the expression in (31). For AIF-TEM to use fewer bits, we require $r_{\text{bits}} > 1$, which leads to $\nu \log_2 K > \log_2 K + \rho$, for $\nu > 1 + \rho/\log_2 K$. \square

To summarize, we demonstrate that under the same parameters κ and δ for both IF-TEM and AIF-TEM, and assuming the conditions in Proposition 1 hold, AIF-TEM not only achieves a lower oversampling rate but also results in smaller quantization error and fewer total bits, as established in Proposition 2.

E. Evaluation results for the Quantization Process

This section presents the simulation results of the quantization process applied to the proposed AIF-TEM and the classical IF-TEM. For AIF-TEM, the evaluation includes both classical and dynamic quantization techniques.

We start by comparing the quantization performance of AIF-TEM and classical IF-TEM with a standard uniform quantizer. The input signals are defined by the equation (20), with Ω varying in the range $2\pi \cdot [10, 50]$ Hz and $M = 2$. The coefficients $a[n]$ are randomly selected 100 times from the interval $[-1, 1]$. The maximum amplitude is calculated as $c_{\text{max}} = \sqrt{(E\Omega)/\pi} = 2$.

Figure 9 shows the MSE due to quantization and reconstruction, as described in (2). The performance of AIF-TEM is depicted by a red line, utilizing parameters $\delta = 0.018$ and $\kappa = 0.21$. β is set to achieve a Nyquist ratio of $r_a = 0.39$, and the MAP block operates (as proposed in Section III-B) with a window of $w = 1$. The weighting factors are configured as $\alpha_1 = 0.98$ and $\alpha_2 = 0.17$ as in

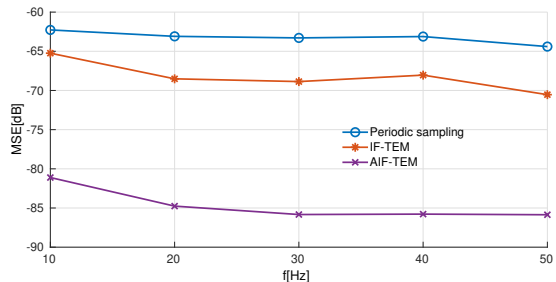


Fig. 9: MSE of Quantization and reconstruction for IF-TEM, AIF-TEM using 12 bits

Section III-E. The blue line represents IF-TEM, configured with the same values of κ and δ . We adjusted b_{IF} to $c_{\text{max}} + \beta$, such that $r_c = 0.39$. The average oversampling rate for IF-TEM is higher than that of AIF-TEM, with ratios of $[4.1, 3.6, 3.2, 2.9, 2.7]$ across frequencies ranging from 10 Hz to 50 Hz. The biases b_n are encoded using 4 bits. Additionally, the total number of bits required for IF-TEM is greater than that of AIF-TEM, with bit usage ratios of $[3.1, 2.7, 2.4, 2.2, 2.0]$.

AIF-TEM clearly outperforms IF-TEM in terms of MSE. It is important to note that in [24], the authors compare IF-TEM with classical sampling under quantization and establish conditions under which the quantization error of IF-TEM is lower than that of the periodic sampler.

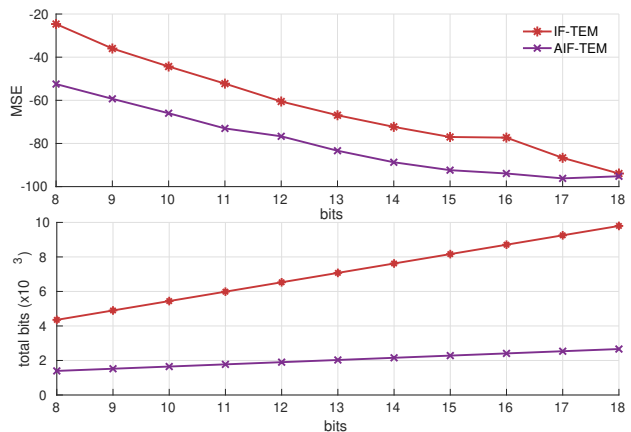


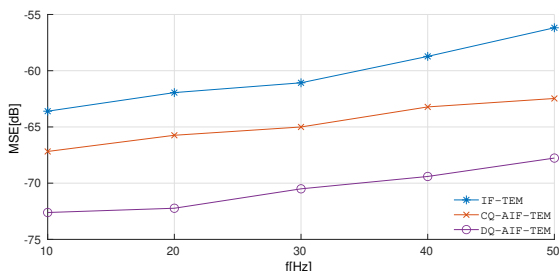
Fig. 10: (a) Comparison in terms of MSE (in dB) between IF-TEM and AIF-TEM. The evaluation includes quantization across different bit levels for T_n , with 3-bit quantization used for the biases in AIF-TEM. (b) Total number of bits required to encode the signal by the samplers.

Figure 10(a) showcases the MSE of quantization for both IF-TEM (red line) and AIF-TEM (purple line). For both samplers, the parameters used are $\delta = 0.0094$ and $\kappa = 0.24$. For AIF-TEM, $\beta = 0.1$ is used, and for IF-TEM, the bias b_{IF} is adjusted to $c_{\text{max}} + \beta$. The number of bits used to encode the biases b_n in AIF-TEM is 3 bits. The oversampling ratio between IF-TEM and AIF-TEM is 4.3, ensuring that the condition of Proposition 2 for a smaller total number of bits in AIF-TEM holds. Figure 10(b) shows the total number of bits required to encode the signal across different bit values used to encode the time differences T_n . The MSE performance of AIF-

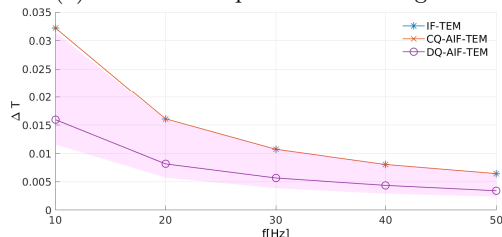
TEM clearly surpasses that of IF-TEM, and AIF-TEM also uses fewer total bits.

Next, we explore the benefits of dynamic quantization for AIF-TEM as detailed in Subsection IV-A, compared to classic quantization for both AIF-TEM and IF-TEM. For this analysis, we use a 2Ω -BL signal, $x(t)$ (where $\Omega = 2\pi[10 : 50]$ Hz), divided into three segments. Each segment i consists of a signal $x_i(t) = a_i \sin(\Omega t)$, with coefficient a_i randomly selected 50 times from the interval $[0, 1]$ for each segment. Each segment is recovered independently using the decoding algorithm described in Section III-C.

The AIF-TEM sampler configuration includes parameters $\kappa = 0.18$, $\beta = 0.1$, and a threshold δ set to achieve a Nyquist ratio $r_a = 0.67$ for each frequency, with the MAP block utilizing a window of $w = 15$. IF-TEM is configured with the same κ and $\delta_c = \delta$, but with a fixed bias $b_{\text{IF}} = c_{\text{max}} + \beta$, ensuring $r_c = r_a = 0.67$. With these settings, the average oversampling rate is 16.25 for IF-TEM and 11.2 for AIF-TEM.



(a) MSE of the quantization using 12 bits.



(b) Dynamic range of time differences, $\Delta T = (T_{\text{max}} - T_{\text{min}})$. The purple line represents the average dynamic range of time differences for each segment i , expressed as $\Delta T_i = (T_{\text{max}}^{(i)} - T_{\text{min}}^{(i)})$, and the shaded region captures the range of ΔT_i .

Fig. 11: Performance comparison of quantization methods for IF-TEM, Classic Quantization for AIF-TEM (CQ-AIF), and Dynamic Quantization for AIF-TEM (DQ-AIF).

Figure 11 illustrates the performance of classic quantization for IF-TEM and both classic and dynamic quantization methods for AIF-TEM. Subfigure 11(a) displays the total MSE of quantization and reconstruction, as defined in (2). Subfigure 11(b) shows the dynamic range of time differences denoted by $\Delta T = (T_{\text{max}} - T_{\text{min}})$. The classic quantization performance for IF-TEM is indicated by the blue line, as described in Section IV-B, which uses a fixed quantization step across all segments, given by equation (25). For AIF-TEM, the red line illustrates the performance of classic quantization, while the purple line represents dynamic quantization. The dynamic approach varies the quantization step for each segment based on the estimated maximum amplitude calculated per equa-

tion (21). The shaded purple region marks the range of maximum time differences per segment i , as defined in equation (24), which directly impacts the quantization step size. Here, T_{max} is calculated based on (23), with the estimated amplitude \hat{c}_n .

Dynamic quantization significantly improves MSE performance, reducing it by at least 6 dB compared to classic quantization for AIF-TEM and by at least 10 dB compared to IF-TEM.

Sam.	Segment A			Segment B			Segment C		
	M	B	ΔT	M	B	ΔT	M	B	ΔT
IF.	-64	-43	4.5	-64	-43	4.5	-73	-43	4.5
AIF.	-63	-59	3.1	-69	-62	3.1	-75	-69	3.1
DAI.	-63	-59	3.1	-74	-72	1.8	-89	-82	1.3

TABLE I: Comparative performance with BL signal. The table represents the MSE in dB (M) of recovery for each quantizer (classic quantization for IF-TEM (IF), AIF-TEM (AIF), and dynamic quantization for AIF-TEM (DAI)), the MSE bound in dB (B), and the dynamic range of time differences (ΔT) in sec (10^{-2}) for each segment of the signal.

Table I illustrates the performance of classic quantization for IF-TEM and both classic and dynamic quantization methods for AIF-TEM. Using the same signal as in Figure I, for each segment, the table represents the MSE of quantization and the MSE bound given in equation (29) with the estimated amplitude for AIF-TEM and fixed bias and maximum amplitude c_{max} for IF-TEM. Dynamic quantization improves MSE performance and reduces the quantization step size based on the amplitude of each segment.

V. Conclusion

This paper introduces an Adaptive Integrate-and-Fire Time Encoding Machine (AIF-TEM) that extends classical IF-TEM by dynamically adapting the bias according to temporal signal amplitude variations. The proposed design addresses the oversampling inefficiency of fixed-bias IF-TEM, where the bias is independent of the temporal signal amplitude and may lead to excessive sampling density when the input amplitude is low. We established analytical conditions for correct adaptive operation, including the MAP condition (i.e., maintaining the adaptive bias slightly above, yet close to, the temporal maximum amplitude of the input signal) and the segment-wise Nyquist constraint (i.e., maximum Nyquist ratio smaller than one), ensuring stable encoding and reconstruction. Closed-form bounds were derived for reconstruction distortion and quantization error, characterizing their dependence on the adaptive bias, sampling density, and segment length. The analysis and simulations demonstrate that the proposed adaptive strategy significantly reduces oversampling rate, mean-squared reconstruction error, and total bit usage compared to fixed-bias IF-TEM and periodic sampling under identical signal conditions. These results show that a simple causal MAP implementation is sufficient to achieve consistent rate-distortion improvements while preserving reconstruction guarantees for bandlimited inputs. Future work will consider alternative bias estimation strategies

and extensions to broader signal classes and hardware-aware implementations, including mechanisms that further enforce the correct MAP operation condition under model uncertainty or transient estimation errors.

References

- [1] A. Omar and A. Cohen, "Adaptive Integrate-and-Fire Time Encoding Machine," in 2024 32nd European Signal Processing Conference (EUSIPCO). IEEE, 2024, pp. 2442–2446.
- [2] A. Antoniou, *Digital signal processing*. McGraw-Hill, 2006.
- [3] M. Miskowicz, *Event-based control and signal processing*. CRC press, 2018.
- [4] D. Wei, V. Garg, and J. G. Harris, "An asynchronous delta-sigma converter implementation," in 2006 IEEE Int. Symp. on Cir. and Sys. (ISCAS). IEEE, 2006, pp. 4–pp.
- [5] D. Chen, Y. Li, D. Xu, J. G. Harris, and J. C. Principe, "Asynchronous biphasic pulse signal coding and its CMOS realization," in 2006 IEEE Int. Symp. on Cir. and Sys. (ISCAS). IEEE, 2006, pp. 4–pp.
- [6] K. Kozmin, J. Johansson, and J. Delsing, "Level-crossing ADC performance evaluation toward ultrasound application," *IEEE Transactions on Circuits and Systems I: Regular Papers*, vol. 56, no. 8, pp. 1708–1719, 2008.
- [7] F. Akopyan, R. Manohar, and A. B. Apsel, "A level-crossing flash asynchronous analog-to-digital converter," in 12th IEEE International Symposium on Asynchronous Circuits and Systems (ASYNC'06). IEEE, 2006, pp. 11–pp.
- [8] M. Saeed, Q. Wang, O. Märtens, B. Larras, A. Frappé, B. Cardiff, and D. John, "Evaluation of level-crossing ADCs for event-driven ECG classification," *IEEE Transactions on Biomedical Circuits and Systems*, vol. 15, no. 6, pp. 1129–1139, 2021.
- [9] A. A. Lazar and L. T. Tóth, "Perfect recovery and sensitivity analysis of time encoded bandlimited signals," *IEEE Trans. on Circ. and Sys. I: Regular Papers*, vol. 51, no. 10, pp. 2060–2073, 2004.
- [10] A. A. Lazar, E. K. Simonyi, and L. T. Tóth, "Time encoding of bandlimited signals, an overview," in *Proceedings of conference on telecommunication systems, modeling and analysis*. Citeseer, 2005.
- [11] S. Rudresh, A. J. Kamath, and C. S. Seelamantula, "A time-based sampling framework for finite-rate-of-innovation signals," in 2020 IEEE ICASSP. IEEE, 2020, pp. 5585–5589.
- [12] D. Koscielnik and M. Miskowicz, "Designing time-to-digital converter for asynchronous ADCs," in 2007 IEEE Design and Diagnostics of Electronic Circ. and Sys. IEEE, 2007, pp. 1–6.
- [13] D. Florescu and A. Bhandari, "Time encoding via unlimited sampling: Theory, algorithms and hardware validation," *IEEE Trans. on Signal Processing*, vol. 70, pp. 4912–4924, 2022.
- [14] P. R. Kinget, A. A. Lazar, and L. T. Tóth, "On the robustness of an analog VLSI implementation of a time encoding machine," in 2005 IEEE Int. Symp. on Cir. and Sys. IEEE, 2005, pp. 4221–4224.
- [15] D. Gontier and M. Vetterli, "Sampling based on timing: Time encoding machines on shift-invariant subspaces," *Applied and Computational Harmonic Analysis*, vol. 36, no. 1, pp. 63–78, 2014.
- [16] H. Naaman, S. Mulleti, and Y. C. Eldar, "FRI-TEM: Time encoding sampling of finite-rate-of-innovation signals," *IEEE Transactions on Signal Processing*, vol. 70, pp. 2267–2279, 2022.
- [17] M. Rastogi, A. S. Alvarado, J. G. Harris, and J. C. Principe, "Integrate and fire circuit as an ADC replacement," in 2011 IEEE Int. Symp. on Cir. and Sys. (ISCAS). IEEE, 2011, pp. 2421–2424.
- [18] A. A. Lazar, "Time encoding with an integrate-and-fire neuron with a refractory period," *Neurocomputing*, vol. 58, pp. 53–58, 2004.
- [19] S. Ryu, C. Y. Park, W. Kim, S. Son, and J. Kim, "A time-based pipelined ADC using integrate-and-fire multiplying-DAC," *IEEE Trans. on Circ. and Sys. I: Regular Papers*, vol. 68, no. 7, pp. 2876–2889, 2021.
- [20] K. Adam, A. Scholefield, and M. Vetterli, "Sampling and reconstruction of bandlimited signals with multi-channel time encoding," *IEEE Trans. on Signal Processing*, vol. 68, pp. 1105–1119, 2020.
- [21] S. Tarnopolsky, H. Naaman, Y. C. Eldar, and A. Cohen, "Compressed IF-TEM: Time Encoding Analog-To-Digital Compression," *arXiv preprint arXiv:2210.17544*, 2022.
- [22] D. Kościelnik, D. Rzepka, and J. Szyduczyński, "Sample-and-hold asynchronous sigma-delta time encoding machine," *IEEE Trans. on Circ. and Sys. II: Express Briefs*, vol. 63, no. 4, pp. 366–370, 2015.
- [23] R. Guo and A. Bhandari, "ED-FreEst: Event-Driven Frequency Estimation," in 2024 32nd European Signal Processing Conference (EUSIPCO). IEEE, 2024, pp. 867–871.
- [24] H. Naaman, S. Mulleti, Y. C. Eldar, and A. Cohen, "Time-based quantization for FRI and bandlimited signals," in 2022 30th European Signal Processing Conference (EUSIPCO), pp. 2241–2245, 2022.
- [25] D. Florescu, "Model-driven quantization for time encoding machines," in 2023 International Conference on Sampling Theory and Applications (SampTA). IEEE, 2023, pp. 1–5.
- [26] D. Kościelnik, M. Miśkiewicz, and M. Jabłeka, "Natural compression and expansion characteristics of asynchronous sigma-delta ADC," in 2011 5th International Conference on Signal Processing and Communication Systems (ICSPCS). IEEE, 2011, pp. 1–8.
- [27] A. Papoulis, "Limits on bandlimited signals," *Proceedings of the IEEE*, vol. 55, no. 10, pp. 1677–1686, 1967.
- [28] A. M. Andrew, "Spiking neuron models: Single neurons, populations, plasticity," *Kybernetes*, 2003.
- [29] N. Fourcaud-Trocmé, D. Hansel, C. Van Vreeswijk, and N. Brunel, "How spike generation mechanisms determine the neuronal response to fluctuating inputs," *Journal of neuroscience*, vol. 23, no. 37, pp. 11628–11640, 2003.
- [30] R. Brette and W. Gerstner, "Adaptive exponential integrate-and-fire model as an effective description of neuronal activity," *Journal of neurophysiology*, vol. 94, no. 5, pp. 3637–3642, 2005.
- [31] Y.-H. Liu and X.-J. Wang, "Spike-frequency adaptation of a generalized leaky integrate-and-fire model neuron," *Journal of computational neuroscience*, vol. 10, pp. 25–45, 2001.
- [32] M.-W. Kwon, K. Park, and B.-G. Park, "Low-power adaptive integrate-and-fire neuron circuit using positive feedback FET Co-Integrated with CMOS," *IEEE Access*, vol. 9, pp. 159925–159932, 2021.
- [33] S. Millner, A. Grübl, K. Meier, J. Schemmel, and M.-O. Schwartz, "A VLSI implementation of the adaptive exponential integrate-and-fire neuron model," *Advances in neural information processing systems*, vol. 23, 2010.
- [34] M. Davies, N. Srinivasa, T.-H. Lin, G. Chinya, Y. Cao, S. H. Choday, G. Dimou, P. Joshi, N. Imam, S. Jain et al., "Loihi: A neuromorphic manycore processor with on-chip learning," *IEEE Micro*, vol. 38, no. 1, pp. 82–99, 2018.
- [35] C. Kikkert and M. P.J., "Asynchronous delta sigma modulation." 1975.
- [36] R. B. Stein, "A theoretical analysis of neuronal variability," *Biophysical journal*, vol. 5, no. 2, pp. 173–194, 1965.
- [37] K. Ozols, R. Shavelis, and M. Greitans, "Amplitude adaptive asynchronous sigma-delta modulator," in 2013 8th International Symposium on Image and Signal Processing and Analysis (ISPA). IEEE, 2013, pp. 467–470.
- [38] K. Ozols and R. Shavelis, "Amplitude adaptive ASDM without envelope encoding," in 2016 24th European Signal Processing Conference (EUSIPCO). IEEE, 2016, pp. 165–169.
- [39] R. Shavelis, K. Ozols, and M. Greitans, "Amplitude adaptive ASDM circuit," in 2017 3rd International Conference on Event-Based Control, Communication and Signal Processing (EBCCSP). IEEE, 2017, pp. 1–8.
- [40] D. Florescu and D. Coca, "A novel reconstruction framework for time-encoded signals with integrate-and-fire neurons," *Neural computation*, vol. 27, no. 9, pp. 1872–1898, 2015.
- [41] H. Nyquist, "Certain topics in telegraph transmission theory," *Transactions of the American Institute of Electrical Engineers*, vol. 47, no. 2, pp. 617–644, 1928, doi: <https://doi.org/10.1109/T-AIEE.1928.5055024>.
- [42] A. A. Lazar, E. K. Simonyi, and L. T. Tóth, "A real-time algorithm for time decoding machines," in 2006 14th European Signal Processing Conference. IEEE, 2006, pp. 1–5.
- [43] —, "An overcomplete stitching algorithm for time decoding machines," *IEEE Transactions on Circuits and Systems I: Regular Papers*, vol. 55, no. 9, pp. 2619–2630, 2008.

- [44] —, “Fast recovery algorithms for time encoded bandlimited signals,” in Proceedings.(ICASSP’05). IEEE International Conference on Acoustics, Speech, and Signal Processing, 2005., vol. 4. IEEE, 2005, pp. iv–237.
- [45] N. T. Thao, D. Rzepka, and M. Miśkiewicz, “Bandlimited signal reconstruction from leaky integrate-and-fire encoding using pocs,” IEEE Transactions on Signal Processing, vol. 71, pp. 1464–1479, 2023.
- [46] R. Alexandru and P. L. Dragotti, “Reconstructing classes of non-bandlimited signals from time encoded information,” IEEE Transactions on Signal Processing, vol. 68, pp. 747–763, 2019.
- [47] D. Florescu and A. Bhandari, “Time encoding of sparse signals with flexible filters,” in 2023 International Conference on Sampling Theory and Applications (SampTA). IEEE, 2023, pp. 1–5.
- [48] B. Welford, “Note on a method for calculating corrected sums of squares and products,” Technometrics, vol. 4, no. 3, pp. 419–420, 1962.
- [49] J. Xie, C. Li, N. Li, P. Li, X. Wang, D. Gao, D. Yao, P. Xu, G. Yin, and F. Li, “Robust autoregression with exogenous input model for system identification and predicting,” Electronics, vol. 10, no. 6, p. 755, 2021.
- [50] C. K. Chui, G. Chen et al., Kalman filtering. Springer, 2017.
- [51] J. Cioffi and T. Kailath, “Fast, recursive-least-squares transversal filters for adaptive filtering,” IEEE Transactions on Acoustics, Speech, and Signal Processing, vol. 32, no. 2, pp. 304–337, 1984.
- [52] J. Benedetto and M. Frazier, “Theory and practice of irregular sampling,” in Wavelets: Mathematics and Applications. CRC, 1994, pp. 305–363.
- [53] R. J. Duffin and A. C. Schaeffer, “A class of nonharmonic fourier series,” Trans. of the American Math. Society, vol. 72, no. 2, pp. 341–366, 1952.
- [54] P. Sankar and S. Pavan, “Analysis of integrator nonlinearity in a class of continuous-time delta-sigma modulators,” IEEE Transactions on Circuits and Systems II: Express Briefs, vol. 54, no. 12, pp. 1125–1129, 2007.
- [55] M. Mekel, V. Karp, S. Mulleti, and A. Cohen, “Self-calibrating integrate-and-fire time encoding machine,” Accepted for publication in IEEE ICASSP 2026. ArXiv preprint arXiv:2509.10831, 2025.
- [56] A. V. Oppenheim, Discrete-time signal processing. Pearson Education India, 1999.
- [57] F. J. Harris, “On the use of windows for harmonic analysis with the discrete fourier transform,” Proceedings of the IEEE, vol. 66, no. 1, pp. 51–83, 2005.
- [58] A. A. Lazar and L. T. Tóth, “Time encoding and perfect recovery of bandlimited signals,” in 2003 IEEE ICASSP, 2003. Proceedings.(ICASSP’03)., vol. 6. IEEE, 2003, pp. VI–709.
- [59] G. H. Hardy, J. E. Littlewood, and G. Pólya, Inequalities. Cambridge university press, 1952.

Appendix

A. Definitions

Definition 5. The operator \mathcal{G} maps an arbitrary function x into a bandlimited function via $\mathcal{G}x = (g * x)$, where $*$ denotes convolution and $g(t) = \sin(\Omega t)/\pi t$, known as the sinc function.

Definition 6. The operator \mathcal{A}^* is defined by

$$\mathcal{A}^* x = \sum_{n \in \mathbb{Z}} x(\theta_n) \mathcal{G}1_{[t_{n-1}, t_n]}, \quad (32)$$

where $\mathcal{G}1_{[t_{n-1}, t_n]}$ applies the operator \mathcal{G} to a pulse function defined over the interval $[t_{n-1}, t_n]$.

Definition 7. Let $f : \mathbb{R} \rightarrow \mathbb{R}$ and let \mathcal{T} be a general time window defined by $\mathcal{T} = [t_{\text{start}}, t_{\text{end}}]$, with t_{start}

and t_{end} being the start and end points of the window, respectively. The norm $\|f\|_{\mathcal{T}}^2$ is given by

$$\|f\|_{\mathcal{T}}^2 = \int_{t_{\text{start}}}^{t_{\text{end}}} |f(u)|^2 du.$$

Definition 8. Let $f : \mathbb{R} \rightarrow \mathbb{R}, g : \mathbb{R} \rightarrow \mathbb{R}$, the inner product $\langle f, g \rangle_{\mathcal{T}}$ is defined by

$$\langle f, g \rangle_{\mathcal{T}} = \int_{t_{\text{start}}}^{t_{\text{end}}} f(u)g(u)du.$$

B. Windowed Bernstein Inequality with Leakage

Lemma 5 (Windowed Bernstein inequality with leakage). Let $f : \mathbb{R} \rightarrow \mathbb{R}$ be with frequency support $[-\Omega, \Omega]$ and assume $f \in L^2(\mathbb{R})$ (finite energy). Let $\mathcal{T} = [t_s, t_e]$ be a finite time window and define the enlarged window $\mathcal{T}_{\Delta} = [t_s - \Delta, t_e + \Delta]$ for some $\Delta > 0$. Let $\varphi \in C^1(\mathbb{R})$ be a real-valued taper, i.e., a continuously differentiable function, such that $0 \leq \varphi(t) \leq 1$, $\varphi(t) = 1$ for all $t \in \mathcal{T}$, and $\varphi(t) = 0$ for all $t \notin \mathcal{T}_{\Delta}$. Define the tapered signal $g(t) \triangleq f(t)\varphi(t)$ and $G(\omega) = \mathcal{F}\{g\}(\omega)$, and let $\mathcal{R}_{\Delta} \triangleq \mathcal{T}_{\Delta} \setminus \mathcal{T}$. Then

$$\|f'\|_{\mathcal{T}}^2 \leq \Omega^2 \|f\|_{\mathcal{T}}^2 + \mathcal{J}_{\varphi}, \quad (33)$$

where the (nonnegative) leakage term is

$$\begin{aligned} \mathcal{J}_{\varphi} \triangleq & \Omega^2 \|f\|_{\mathcal{R}_{\Delta}}^2 + \frac{1}{2\pi} \int_{|\omega| > \Omega} (\omega^2 - \Omega^2) |G(\omega)|^2 d\omega \\ & + \|f\varphi'\|_2^2 + 2|\langle g', f\varphi' \rangle| \geq 0, \end{aligned} \quad (34)$$

and $\langle \cdot, \cdot \rangle$ denotes the $L^2(\mathbb{R})$ inner product.

In the supplementary material of this work, we provide a discussion on the leakage term and tapering functions in the finite regime considered in signal processing literature.

Proof. Since $\varphi(t) = 0$ for all $t \notin \mathcal{T}_{\Delta}$ and $f \in L^2(\mathbb{R})$, we have $g \in L^2(\mathbb{R})$. Moreover, since $\varphi \in C^1(\mathbb{R})$,

$$g'(t) = f'(t)\varphi(t) + f(t)\varphi'(t),$$

and $g' \in L^2(\mathbb{R})$, so Parseval’s identity applies and $\mathcal{F}\{g'\}(\omega) = j\omega G(\omega)$ in L^2 . Let $\Lambda \triangleq \|f\varphi'\|_2^2 + 2|\langle g', f\varphi' \rangle|$. The proof proceeds as follows

$$\begin{aligned} \|f'\|_{\mathcal{T}}^2 & \stackrel{(a)}{=} \|f' \cdot 1_{\mathcal{T}}\|_2^2 \stackrel{(b)}{\leq} \|f'\varphi\|_2^2 \\ & \stackrel{(c)}{=} \|g' - f\varphi'\|_2^2 \\ & \stackrel{(d)}{=} \|g'\|_2^2 + \|f\varphi'\|_2^2 - 2\text{Re}\langle g', f\varphi' \rangle \\ & \stackrel{(e)}{\leq} \|g'\|_2^2 + \|f\varphi'\|_2^2 + 2|\langle g', f\varphi' \rangle| \\ & \stackrel{(f)}{=} \|g'\|_2^2 + \Lambda \stackrel{(g)}{=} \frac{1}{2\pi} \int_{-\infty}^{\infty} \omega^2 |G(\omega)|^2 d\omega + \Lambda \\ & \stackrel{(h)}{=} \frac{1}{2\pi} \int_{|\omega| \leq \Omega} \omega^2 |G(\omega)|^2 d\omega + \frac{1}{2\pi} \int_{|\omega| > \Omega} \omega^2 |G(\omega)|^2 d\omega + \Lambda \\ & \stackrel{(i)}{\leq} \Omega^2 \frac{1}{2\pi} \int_{|\omega| \leq \Omega} |G(\omega)|^2 d\omega + \frac{1}{2\pi} \int_{|\omega| > \Omega} \omega^2 |G(\omega)|^2 d\omega + \Lambda \\ & \stackrel{(j)}{=} \Omega^2 \frac{1}{2\pi} \int_{-\infty}^{\infty} |G(\omega)|^2 d\omega + \frac{1}{2\pi} \int_{|\omega| > \Omega} (\omega^2 - \Omega^2) |G(\omega)|^2 d\omega + \Lambda \\ & \stackrel{(k)}{=} \Omega^2 \|g\|_2^2 + \frac{1}{2\pi} \int_{|\omega| > \Omega} (\omega^2 - \Omega^2) |G(\omega)|^2 d\omega + \Lambda \\ & \stackrel{(l)}{\leq} \Omega^2 \|f\|_{\mathcal{T}}^2 + \Omega^2 \|f\|_{\mathcal{R}_{\Delta}}^2 + \frac{1}{2\pi} \int_{|\omega| > \Omega} (\omega^2 - \Omega^2) |G(\omega)|^2 d\omega + \Lambda \end{aligned}$$

$$\stackrel{(m)}{=} \Omega^2 \|f\|_{\mathcal{T}}^2 + \mathcal{J}_\varphi.$$

where (a) follows from the definition of the windowed norm, and (b) since $\varphi(t) = 1$ for all $t \in \mathcal{T}$ and $0 \leq \varphi(t) \leq 1$ elsewhere, we have

$$\begin{aligned} \|f'\|_{\mathcal{T}}^2 &= \int_{\mathcal{T}} |f'(t)|^2 dt = \int_{\mathcal{T}} |f'(t)\varphi(t)|^2 dt \\ &\leq \int_{\mathbb{R}} |f'(t)\varphi(t)|^2 dt = \|f'\varphi\|_2^2. \end{aligned}$$

(c) follows since using $g' = f'\varphi + f\varphi'$, we get $f'\varphi = g' - f\varphi'$ and thus $\|f'\varphi\|_2^2 = \|g' - f\varphi'\|_2^2$. (d) expanding the squared norm via the L^2 inner product yields $\|u - v\|_2^2 = \|u\|_2^2 + \|v\|_2^2 - 2\operatorname{Re}\langle u, v \rangle$ with $u = g'$ and $v = f\varphi'$. (e) uses $-\operatorname{Re} z \leq |z|$ for $z \in \mathbb{C}$, hence $-2\operatorname{Re}\langle g', f\varphi' \rangle \leq 2|\langle g', f\varphi' \rangle|$. (f) by the definition of Λ . (g) by Parseval and $\mathcal{F}\{g'\}(\omega) = j\omega G(\omega)$. (h) splitting the integral into in-band and out-of-band parts. (i) follows since $|\omega| \leq \Omega$. (j) is since $\int_{|\omega| < \Omega} \Omega^2 |G|^2 = \int_{-\infty}^{\infty} \Omega^2 |G|^2 - \int_{|\omega| > \Omega} \Omega^2 |G|^2$. (k) by Parseval. (l) using $\varphi = 1$ on \mathcal{T} , $0 \leq \varphi \leq 1$, and $\varphi(t) = 0$ for all $t \notin \mathcal{T}_\Delta$, we have

$$\begin{aligned} \|g\|_2^2 &= \|f\varphi\|_2^2 = \int_{\mathcal{T}} |f(t)|^2 dt + \int_{\mathcal{R}_\Delta} |f(t)|^2 \varphi(t)^2 dt \\ &\leq \|f\|_{\mathcal{T}}^2 + \|f\|_{\mathcal{R}_\Delta}^2. \end{aligned}$$

and substituting this bound for $\|g\|_2^2$ into (k) gives (l).

(m) by the definition of \mathcal{J}_φ in (34) and $\Lambda = \|f\varphi'\|_2^2 + 2|\langle g', f\varphi' \rangle|$. \square

C. The adjoint operator

Lemma 6. Recall operators \mathcal{A} and \mathcal{A}^* as defined in (12) (32), respectively, using the samples in S_{W_i} . For 2Ω -bandlimited signals $x, y \in L_2(\mathbb{R})$, the operators \mathcal{A} and \mathcal{A}^* satisfy

$$\langle \mathcal{A}x, y \rangle = \langle x, \mathcal{A}^*y \rangle,$$

where $\langle \cdot, \cdot \rangle$ denotes the standard $L_2(\mathbb{R})$ inner product.

Proof.

$$\begin{aligned} \langle \mathcal{A}x, y \rangle &= \left\langle \sum_{n \in S_{W_i}} \int_{t_{n-1}}^{t_n} x(u) du g(\cdot - \theta_n), y \right\rangle \\ &\stackrel{(a)}{=} \sum_{n \in S_{W_i}} \int_{t_{n-1}}^{t_n} x(u) du \langle g(\cdot - \theta_n), y \rangle \\ &\stackrel{(b)}{=} \sum_{n \in S_{W_i}} \langle x, \mathbf{1}_{[t_{n-1}, t_n]} \rangle y(\theta_n) \stackrel{(c)}{=} \left\langle x, \sum_{n \in S_{W_i}} y(\theta_n) \mathbf{1}_{[t_{n-1}, t_n]} \right\rangle \\ &\stackrel{(d)}{=} \left\langle \mathcal{G}x, \sum_{n \in S_{W_i}} y(\theta_n) \mathbf{1}_{[t_{n-1}, t_n]} \right\rangle \\ &\stackrel{(e)}{=} \left\langle x, \sum_{n \in S_{W_i}} y(\theta_n) \mathcal{G} \mathbf{1}_{[t_{n-1}, t_n]} \right\rangle = \langle x, \mathcal{A}^*y \rangle \end{aligned}$$

where (a) uses the linearity of the inner product. (b) follows from the exact reproducing property of the sinc kernel in $L_2(\mathbb{R})$ for a bandlimited signal y , i.e., $\langle g(\cdot - \theta_n), y \rangle = y(\theta_n)$, and expressing the integral as an inner product. (c) uses linearity. (d) uses the property $\mathcal{G}x = x$ for 2Ω -bandlimited x . (e) uses the self-adjointness of the orthogonal projector \mathcal{G} . This completes the proof. \square

D. Proof of Lemma 1

Proof of Lemma 1. Recall the operator \mathcal{A} , as defined in (12). To establish an upper bound on the norm of the discrepancy between x and $\mathcal{A}x$ over a time window W_i , we use techniques similar to those in [9, Appendix B] for classical TEM, and in [52] for irregular sampling and grounded in frame theory, as shown in [53]. However, the authors in [9] (as is common in classical recovery schemes, e.g., [18], [58]) provide proof for the norm's upper bound over \mathbb{R} , whereas here we focus on a specific i -th time window W_i , working in the finite regime. Let \mathcal{A}^* denote the adjoint operator of \mathcal{A} , as given in (32) and proved in Lemma 6⁵. Thus, for the finite norm $\|\cdot\|_{W_i}^2$ (see Lemma 5), we have

$$\begin{aligned} \|x - \mathcal{A}^*x\|_{W_i}^2 &= \|x - \sum_{n \in S_{W_i}} x(\theta_n) \mathcal{G} \mathbf{1}_{[t_{n-1}, t_n]}\|_{W_i}^2 \\ &\stackrel{(a)}{=} \|\mathcal{G}x - \sum_{n \in S_{W_i}} x(\theta_n) \mathcal{G} \mathbf{1}_{[t_{n-1}, t_n]}\|_{W_i}^2 \\ &= \|\mathcal{G}(x - \sum_{n \in S_{W_i}} x(\theta_n) \mathbf{1}_{[t_{n-1}, t_n]})\|_{W_i}^2 \\ &\stackrel{(b)}{\leq} \|\mathcal{G}(x - \sum_{n \in S_{W_i}} x(\theta_n) \mathbf{1}_{[t_{n-1}, t_n]})\|_2^2 \\ &\stackrel{(c)}{\leq} \|x - \sum_{n \in S_{W_i}} x(\theta_n) \mathbf{1}_{[t_{n-1}, t_n]}\|_2^2 \\ &\stackrel{(d)}{=} \left\| \sum_{n \in S_{W_i}} [x - x(\theta_n)] \mathbf{1}_{[t_{n-1}, t_n]} \right\|_2^2 \\ &\stackrel{(e)}{=} \sum_{n \in S_{W_i}} \int_{t_{n-1}}^{t_n} |x(u) - x(\theta_n)|^2 du \\ &\stackrel{(f)}{\leq} \sum_{n \in S_{W_i}} \frac{4}{\pi^2} (\theta_n - t_{n-1})^2 \int_{t_{n-1}}^{\theta_n} |x'(u)|^2 du \\ &\quad + \frac{4}{\pi^2} (t_n - \theta_n)^2 \int_{\theta_n}^{t_n} |x'(u)|^2 du, \end{aligned}$$

where, (a) follows since x is bandlimited to the support $[-\Omega, \Omega]$, and the operator \mathcal{G} is defined in Appendix A, Definition 5. The function g , as given in Definition 5, is the ideal low-pass filter with the same bandwidth. Consequently, the convolution $\mathcal{G}x = (g * x)$ acts as an identity operator in this bandlimited space, resulting in $\mathcal{G}x = x$. (b) follows from $\|v\|_{W_i} \leq \|v\|_2$ for any $v \in L_2(\mathbb{R})$, and (c) follows because \mathcal{G} is the orthogonal projector onto the bandlimited subspace and is therefore non-expansive in $L_2(\mathbb{R})$. The inequality uses the fact that $\|v\|_{W_i} \leq \|v\|_2$ for any $v \in L_2(\mathbb{R})$, allowing the global L_2 projector property of \mathcal{G} to be applied before restricting the bound to the window W_i . (d) follows by regrouping the terms. The restriction to the finite segment W_i is interpreted together with the leakage control of Lemma 5, which accounts for the residual boundary effects introduced by the finite-window localization through the term $\mathcal{J}_{\varphi_i}(x)$. (e) follows

⁵The adjoint relation is established with respect to the global $L_2(\mathbb{R})$ inner product. The windowed norm satisfies $\|v\|_{W_i} \leq \|v\|_2$, so bounds derived in $L_2(\mathbb{R})$ remain valid when restricted to the segment W_i .

since the intervals $[t_{n-1}, t_n]$, $n \in S_{W_i}$, are disjoint. (f) follows by applying Wirtinger's inequality [9].

We do note that since for any $n \in S_{W_i}$

$$(\theta_n - t_{n-1})^2 = (t_n - \theta_n)^2 = \frac{(t_n - t_{n-1})^2}{4},$$

we obtain

$$\begin{aligned} \|x - \mathcal{A}^* x\|_{W_i}^2 &\leq \sum_{n \in S_{W_i}} \frac{1}{\pi^2} (t_n - t_{n-1})^2 \int_{t_{n-1}}^{t_n} |x'(u)|^2 du \\ &\leq \frac{1}{\pi^2} \left(\max_{n \in S_{W_i}} (T_n) \right)^2 \sum_{n \in S_{W_i}} \int_{t_{n-1}}^{t_n} |x'(u)|^2 du \\ &= \frac{1}{\pi^2} \left(\max_{n \in S_{W_i}} (T_n) \right)^2 \|x'\|_{W_i}^2 \\ &\stackrel{(h)}{\leq} \frac{1}{\pi^2} \left(\max_{n \in S_{W_i}} (T_n) \right)^2 \left(\Omega^2 \|x\|_{W_i}^2 + \mathcal{J}_{\varphi_i}(x) \right), \end{aligned}$$

where (h) follows from Lemma 5, applied to the bandlimited signal x over the window W_i (with the associated taper φ_i). Finally, substituting the bound $\max_{n \in S_{W_i}} T_n \leq r_{w_i} \frac{\pi}{\Omega}$, where $r_{w_i} = \max_{n \in S_{W_i}} \{r_{a_n}\}$ and r_{a_n} is defined in (13), and using the windowed Bernstein inequality with leakage (Lemma 5), we obtain

$$\|x - \mathcal{A}x\|_{W_i}^2 \leq r_{w_i}^2 \left(\|x\|_{W_i}^2 + \frac{1}{\Omega^2} \mathcal{J}_{\varphi_i}(x) \right).$$

This completes the proof of the lemma. \square

E. Proof of Lemma 2

Proof of Lemma 2. The recovered signal for segment W_i , x_{L_i} , is defined by (14), with $l = L_i$. We evaluate the norm difference between the original signal x and the recovered signal x_{L_i} over the segment W_i as follows

$$\|x - x_{L_i}\|_{W_i} = \|x - \sum_{n=0}^{L_i} (I - \mathcal{A})^n \mathcal{A}x\|_{W_i} = \|(I - \mathcal{A})^{L_i+1} x\|_{W_i},$$

where the last equality follows from the finite telescoping identity $I = \sum_{n=0}^{L_i} (I - \mathcal{A})^n \mathcal{A} + (I - \mathcal{A})^{L_i+1}$. This completed the lemma proof. \square

Lemma 7. Assume a 2Ω -BL, c_{\max} -bounded signal $x \in L^2(\mathbb{R})$ with finite energy E , sampled using an AIF-TEM. Then, the norm of the discrepancy between x and $\mathcal{A}x$ over the entire real line is bounded by $\|x - \mathcal{A}x\|_2 \leq r_{w_i} \|x\|_2$, where \mathcal{A} is defined in (12) and $r_{w_i} = \max_{n \in S_{W_i}} r_{a_n} < 1$.

Proof. The proof follows the same steps as in [9, Appendix B]. Since the operator \mathcal{A} is constructed using only the sampling intervals indexed by $n \in S_{W_i}$, the worst-case interval length satisfies $\max_{n \in S_{W_i}} T_n \leq r_{w_i} \frac{\pi}{\Omega}$, which yields the stated $L^2(\mathbb{R})$ error bound. \square

F. Key Mathematical Tools

1) Observation 1: Assume the quantization error $d_n = (\tilde{T}_n - T_n)$ is a sequence of i.i.d. random variables in $[-\Delta_i/2, \Delta_i/2]$. Then $\mathbb{E}[\epsilon_n \epsilon_m] = \left(\frac{\kappa\delta}{T_n}\right)^2 \frac{\Delta_i^2}{12} \delta_{n,m}$.

Proof.

$$\epsilon_n = (\kappa\delta - b_n \tilde{T}_n) - \int_{\tilde{t}_{n-1}}^{\tilde{t}_n} x(u) du$$

$$\begin{aligned} &= \kappa\delta - b_n T_n + b_n T_n - b_n \tilde{T}_n - \int_{\tilde{t}_{n-1}}^{\tilde{t}_n} x(u) du \\ &= \int_{t_{n-1}}^{t_n} x(u) du - \int_{\tilde{t}_{n-1}}^{\tilde{t}_n} x(u) du - b_n (\tilde{T}_n - T_n) \\ &\stackrel{a}{=} x(\zeta_n) T_n - x(\hat{\zeta}_n) \tilde{T}_n - b_n (\tilde{T}_n - T_n) \\ &\stackrel{b}{\simeq} (-x(\zeta_n) - b_n) (\tilde{T}_n - T_n) \stackrel{c}{=} -\frac{\kappa\delta}{T_n} (\tilde{T}_n - T_n), \end{aligned}$$

where (a) follows from the mean value theorem. (b) follows from the approximation used in [9, Appendix C]. Where $\zeta_n \in (t_{n-1}, t_n)$ and $\hat{\zeta}_n \in (\tilde{t}_{n-1}, \tilde{t}_n)$, for sufficiently small Δ_i , we get $\hat{\zeta}_n \simeq \zeta_n$. (c) follows because $x(\zeta_n) = \frac{1}{T_n} \int_{t_{n-1}}^{t_n} x(u) du = \frac{\kappa\delta}{T_n} - b_n$.

Let $d_n = (\tilde{T}_n - T_n)$, this leads to

$$\mathbb{E}[\epsilon_n \epsilon_m] = \frac{\kappa\delta}{T_n} \frac{\kappa\delta}{T_m} \mathbb{E}[d_n d_m] \stackrel{(a)}{=} \left(\frac{\kappa\delta}{T_n}\right)^2 \frac{\Delta_i^2}{12} \delta_{n,m},$$

where (a) follows since the quantization error $d_n = (\tilde{T}_n - T_n)$ is a sequence of i.i.d. random variables uniformly distributed in $[-\Delta_i/2, \Delta_i/2]$. Therefore, $\mathbb{E}[d_n d_m] = \frac{\Delta_i^2}{12} \delta_{n,m}$. \square

2) Observation 2: For any positive numbers $T_n, \forall n \in S_{W_i}$,

$$(1/\overline{T_n}) \overline{(1/T_n)^2} \leq \overline{(1/T_n)^3}.$$

Proof. First, since $T_n > 0$ for all $n \in S_{W_i}$, the harmonic–arithmetic mean inequality gives $(1/\overline{T_n}) \leq \overline{(1/T_n)}$. Thus, it is enough to show that

$$\overline{(1/\overline{T_n}) \overline{(1/T_n)^2}} \leq \overline{(1/T_n)^3}.$$

Let $a_n \triangleq 1/T_n$, for $n \in S_{W_i}$ and $L_i = |S_{W_i}|$. Then the required inequality becomes

$$\left(\frac{1}{L_i} \sum_{n \in S_{W_i}} a_n\right) \left(\frac{1}{L_i} \sum_{n \in S_{W_i}} a_n^2\right) \leq \frac{1}{L_i} \sum_{n \in S_{W_i}} a_n^3.$$

Multiplying both sides by L_i^2 , and applying the Cauchy–Schwarz and Hölder inequalities [59], yields

$$\left(\sum_{n \in S_{W_i}} a_n\right) \left(\sum_{n \in S_{W_i}} a_n^2\right) \leq L_i \sum_{n \in S_{W_i}} a_n^3.$$

Now, observe that

$$\begin{aligned} L_i \sum_{n \in S_{W_i}} a_n^3 - \left(\sum_{n \in S_{W_i}} a_n\right) \left(\sum_{n \in S_{W_i}} a_n^2\right) \\ = \frac{1}{2} \sum_{n \in S_{W_i}} \sum_{m \in S_{W_i}} (a_n - a_m)^2 (a_n + a_m). \end{aligned}$$

Since $a_n + a_m > 0$ and $(a_n - a_m)^2 \geq 0$, the right-hand side is nonnegative. Therefore,

$$\left(\sum_{n \in S_{W_i}} a_n\right) \left(\sum_{n \in S_{W_i}} a_n^2\right) \leq L_i \sum_{n \in S_{W_i}} a_n^3,$$

⁶The analyses here treat the adaptive bias values b_n as known at the decoder. This is consistent with the synchronization mechanism described in Sections III-C and IV.

which implies $\overline{(1/T_n)} \overline{(1/T_n)^2} \leq \overline{(1/T_n)^3}$. Combining this with $(1/T_n) \leq \overline{(1/T_n)}$ completes the proof. \square

Supplementary Materials

Leakage Term & Tapering Functions in the Finite Regime

The reconstruction distortion bound in Theorem 1 consists of a classical sampling term and an additional leakage term. The additional leakage term in Lemma 5 and Theorem 1 captures boundary effects arising from finite-window reconstruction. Unlike the classical Bernstein inequality, which provides bounds over the entire real line \mathbb{R} , the present analysis localizes the inequality to finite time segments. This localization enables segment-wise error control but necessarily introduces additional energy contributions. Specifically, these contributions originate from the transition regions surrounding each segment, as well as from spectral spreading outside the nominal frequency band.

The leakage term \mathcal{J}_φ in Lemma 5 consists of two main components. The first component represents signal energy in the transition region $\mathcal{R}_\Delta \triangleq \mathcal{T}_\Delta \setminus \mathcal{T}$, while the second component accounts for spectral leakage induced by windowing. The integral term $\frac{1}{2\pi} \int_{|\omega|>\Omega} (\omega^2 - \Omega^2) |G(\omega)|^2 d\omega$ captures spectral leakage introduced by tapering. Although f is Ω -bandlimited, the tapered signal $g = f\varphi$ is generally not. This phenomenon is analogous to the spectral leakage observed in classical windowed sampling and short-time Fourier analysis. Classical signal processing literature [56] explains spectral leakage as an inherent consequence of windowing: multiplying a signal by a finite-duration window (or taper) corresponds in the frequency domain to convolution with the window spectrum, which generally results in energy spreading outside the nominal signal bandwidth. Different window shapes exhibit different leakage behavior, governed by the tradeoff between main-lobe width and side-lobe decay. Smooth tapers lead to faster spectral decay and reduced out-of-band energy compared to rectangular windows. This effect is extensively analyzed in classical window studies [57], which compares multiple window families and demonstrates how increasing smoothness (e.g., cosine-tapered and Tukey windows) systematically reduces spectral leakage.

The taper used in Lemma 5 belongs to the family of smooth, compactly supported windows studied in the classical window analysis literature, including cosine-tapered (Tukey-type) windows. A closely related construction appears in the work of [42], where smooth overlapping windows are employed to stitch together local reconstructions in time-encoding machines. In that work, windowing is explicitly acknowledged to introduce bandwidth expansion, which is controlled through taper smoothness, window overlap, and post-filtering. In particular, the terms $\Omega^2 \|f\|_{\mathcal{R}_\Delta}^2 + \|f\varphi'\|_2^2 + 2|\langle g', f\varphi' \rangle|$ characterize time-domain leakage effects. The term $\Omega^2 \|f\|_{\mathcal{R}_\Delta}^2$ quantifies the signal energy outside the target segment, whereas $\|f\varphi'\|_2^2$

depends on the derivative of the taper and is supported only in the transition region, since $\varphi = 1$ on \mathcal{T} . The cross term $|\langle g', f\varphi' \rangle|$ can be bounded using the Cauchy–Schwarz inequality, yielding $2|\langle g', f\varphi' \rangle| \leq 2\|g'\|_2 \|f\varphi'\|_2$, and therefore also depends on the taper derivative and is supported only in the transition region. The first contribution generally increases with the transition width Δ , since a wider transition region contains more signal energy. In contrast, the second and third contributions depend on the smoothness of the taper. For standard smooth tapers (e.g., raised-cosine or polynomial tapers), $\|\varphi'\|_\infty = O(\Delta^{-1})$, implying that these terms decrease as the transition width Δ increases for fixed signal energy. In practical settings, the leakage term \mathcal{J}_φ remains small compared to the principal term $\Omega^2 \|f\|_{\mathcal{T}}^2$ when the signal energy in the transition region is limited, and the taper function varies smoothly. In particular, if $\|f\|_{\mathcal{R}_\Delta}^2 \ll \|f\|_{\mathcal{T}}^2$ and $\|\varphi'\|_\infty$ is small, then the time domain leakage components are negligible. This situation occurs when the plateau region of the window (where $\varphi(t) = 1$ for $t \in \mathcal{T}$), i.e., the duration $t_e - t_s$, is large relative to the transition width Δ , so that the boundary region occupies only a small fraction of the segment. Moreover, smooth tapers reduce spectral spreading and control the frequency-domain contribution. In this regime, the inequality in (33) closely approximates the classical Bernstein bound.

In practice, the leakage contribution becomes small when the plateau region (where $\varphi(t) = 1$ for $t \in \mathcal{T}$), i.e., $t_e - t_s$ of the window is large relative to the transition width Δ . In this regime, the boundary region occupies only a small fraction of the segment, and the dominant term in (33) remains $\Omega^2 \|f\|_{\mathcal{T}}^2$, closely approximating the classical Bernstein inequality. In the idealized infinite-domain setting, or asymptotically for sufficiently large segments with smooth tapering, the leakage term can be made arbitrarily small and the bound approaches the classical Bernstein inequality. The leakage term appearing in our distortion analysis, therefore, captures a fundamental and well-understood effect of windowing, consistent with classical digital signal processing theory, window analysis literature, and prior TEM reconstruction frameworks.